Biomarker and pollen evidence for late Pleistocene pluvials in the Mojave Desert

Mark D. Peaple[1], Tripti Bhattacharya[2], Tim K. Lowenstein[3], David McGee[4], Kristian J. Olson[3], Justin S. Stroup[5], Jessica E. Tierney[6], Sarah J. Feakins[1]

[1]Department of Earth Sciences, University of Southern California, Los Angeles, CA 90089

[2]Department of Earth and Environmental Sciences, Syracuse University, Syracuse NY 13210

[3]Department of Geological Sciences and Environmental Studies, State University of New York, Binghamton, New York 13902, USA

[4]Department of Earth, Atmospheric and Planetary Sciences, Massachusetts Institute of Technology, Cambridge, MA 02139

[5]Department of Atmospheric and Geological Sciences, State University of New York at Oswego, Oswego, NY 13126

[6]Department of Geosciences, University of Arizona, Tucson, AZ 85721

Key points

- Biomarker and pollen record from Searles Lake, CA sediment core spanning 200 kyr
- Changes in plant wax hydrogen isotopes consistent with regional speleothems
- Archaeal lipids reveal lake highstands, Termination 2 wetter than Termination 1

Abstract

The climate of the southwestern North America has experienced profound changes between wet and dry phases over the past 200 kyr. To better constrain the timing, magnitude and paleoenvironmental impacts of these changes in hydroclimate, we conducted a multiproxy biomarker study from samples collected from a new 76 m sediment core (SLAPP-SRLS17) drilled in Searles Lake, California. Here, we use biomarkers and pollen to reconstruct vegetation, lake conditions and climate. We find that δD values of long chain *n*-alkanes are dominated by glacial to interglacial changes that match nearby Devils Hole calcite $\delta^{18}O$ variability, suggesting both archives predominantly reflect precipitation isotopes. However, precipitation isotopes do not simply covary with evidence for wet-dry changes in vegetation

and lake conditions, indicating a partial disconnect between large scale atmospheric circulation tracked by precipitation isotopes and landscape moisture availability. Increased crenarchaeol production and decreased evidence for methane cycling reveal a 10 kyr interval of a fresh, productive and well-mixed lake during Termination II, corroborating evidence for a paleolake highstand from shorelines and spillover deposits in downstream Panamint Basin and Death Valley during the end of the penultimate (Tahoe) glacial (140–130 ka). At the same time brGDGTs yield the lowest temperature estimates (mean months above freezing = 9 ± 3°C) of the 200 kyr record. These limnological conditions are not replicated elsewhere in the 200 kyr record, suggesting that the Heinrich stadial 11 highstand was wetter than the last glacial maximum and Heinrich 1 (18–15 ka).

Keywords: plant wax; GDGTs; hydrogen isotopes; carbon isotopes; pollen

Plain language summary

Searles Valley in the Mojave Desert, California, contains a saltpan, the remnants of a former lake. Shoreline features show that the former lake was at times 274 m deep. We studied the ancient lake mud and salt deposits below the valley floor to a depth of 76 m in a sediment core drilled in 2017. The remains of microbes and plants allow us to reconstruct past climate conditions. We find that during cooler glacial periods, conifer forests covered the landscape and plant wax in the core records rainfall that is chemically different from today. These differences are similarly recorded in nearby cave deposits, suggesting changing storm tracks. The wettest climates were found in the cool climate of the penultimate glacial (about 135 000 years ago) when Searles Lake vigorously overflowed into Panamint Basin and Death Valley.

1. Introduction

There is considerable concern over water availability in southwestern North America and

uncertainties around precipitation in climate model projections (Pierce et al., 2013). Proxy reconstructions of past moisture availability under different temperature regimes can help to understand the changing water balance (P–E) during periods of climate change (McGee, 2020), including evidence for water table rise and fall in southwestern North America detected during recent glacial cycles (Wendt et al., 2018).

However, available proxy evidence from southwestern North America suggests different magnitudes of variability and climate change during the late Pleistocene. For instance, Devils Hole and the Leviathan composite record (Figure 1a) are high-resolution speleothem $\delta^{18}O$ records that record glacial-interglacial changes in $\delta^{18}O$ of precipitation over two glacial cycles (Lachniet, 2016; Moseley et al., 2016). However, the magnitudes of variability are larger, and precessional pacing is more strongly represented in the Leviathan composite record than in the Devils Hole calcite. Differences in aquifer mixing, karstic dissolution, and calcite precipitation processes (including temperature) lead to differences between $\delta^{18}O_{calcite}$ in the different cave systems and speleothem types. Independent evidence for precipitation isotopic composition for the last glacial is available from groundwater, studied further south in San Diego, but only for the last glacial (Kulongoski et al., 2009; Seltzer et al., 2021).

Lake sediments provide another archive of precipitation isotopes; for example, the late glacial plant wax δD record from Lake Elsinore, California (Figure 1a) (Feakins et al., 2019). Biomarker studies of Lake Elsinore sediments, specifically bacterial membrane lipids, also yielded evidence of previously unrecognized, highly-variable lake temperatures during the last glacial period (Feakins et al., 2019). However, the 33 ka age range precluded analysis of longer-term trends. Fossil pollen in Lake Elsinore and Searles Lake sediment cores provide evidence for past vegetation and yield insights into past hydroclimate (Heusser et al., 2015;

75 Litwin et al., 1999). However, vegetation composition can be influenced by multiple
76 variables (e.g., temperature, pCO_2, and rainfall).

77 Here we revisit lacustrine sediments from Searles Lake (Figure 1c) to generate a 200 kyr
78 biomarker and pollen reconstruction of limnology as well as regional climate and
79 environmental changes. The combination of plant wax and pollen allows us to independently
80 infer changes in regional precipitation δD and vegetation, which act as tracers for changes in
81 rainfall seasonality in this region. In addition, we analyze a suite of microbial biomarkers to
82 reconstruct aridity and inform on lake salinity, depth, and temperature. The multi-proxy
83 dataset (Table 1) uniquely yields new insights into the timing and magnitude of past changes
84 between aridity and pluvials that filled the chain of lakes to the east of the Sierra Nevada
85 Mountains (Figure 1b) in what is today part of the hyperarid Mojave Desert.

86 **1.1. Regional setting**

87 Searles Valley is an endorheic basin located in the Mojave Desert in southeastern California
88 (Figure 1). Below the evaporites on the valley floor, there are lacustrine muds from past deep
89 lake conditions. Shoreline tufa deposits indicate the lake was formerly up to ~300 m deep
90 (Smith et al., 1983). During past wet climate states, the Owens River carried spillover from
91 the upstream Owens Lake to China Lake and Searles Lake (Figure 1c). Owens Lake receives
92 snowmelt runoff from the eastern flanks of the Sierra Nevada Mountains (Bischoff &
93 Cummins, 2001). Over the past 200 ka, the Owens River has been almost continuously
94 inflowing into Searles Lake, with only the late Holocene and 6 brief (<1 ka) periods during
95 the late glacial receiving no inflow (Bacon et al., 2020). Once between 190 and 130 ka, the
96 catchment may have briefly expanded to include that of Mono Lake (Reheis et al., 2002).
97 When Searles Lake reached 696 m above sea level (asl), it would also reach the spillway into

Panamint Basin and ultimately Death Valley (Forester et al., 2005).

The present-day climate in Searles Valley is hyperarid, with a mean annual precipitation of 100 mm between 1920 – 2016 (Western Regional Climate Center, 2022). Modern monthly mean temperature averages 27.4°C in summer (JJA) and 11.4°C in winter (DJF), with recorded temperature extremes of 41.0°C and -0.8°C (Western Regional Climate Center, 2022). Hot, dry, and often windy conditions promote high potential evaporation ~2000 mm/yr, far in excess of precipitation. Sporadic precipitation is winter-dominated, with DJF and JAS monthly means of 18 mm and 4 mm, respectively (Western Regional Climate Center, 2022). During pluvial conditions, Searles would receive precipitation falling on the Eastern Sierra Nevada through Owens River inflow. Modern Eastern Sierra precipitation also has a winter dominance with DJF and JAS monthly means of 67 mm and 16 mm, respectively (Lake Sabrina) (Western Regional Climate Center, 2022). Local winter precipitation is sourced from storms that derive from the North Pacific and sub-tropical atmospheric rivers (Friedman et al., 1992). Summer rain is sourced from the Gulf of California and Gulf of Mexico at the northern limits of incursion of the North American Monsoon, with a small contribution from North Pacific moisture (Friedman et al., 1992). The isotopic composition of precipitation can be affected by the precipitation moisture source (Dansgaard, 1964). Precipitation from northerly winter and summer storms is typically more D-depleted than southerly sourced moisture in either winter or summer (Friedman et al., 2002), with Searles Valley precipitation having mean summer (March to September) and winter (October to April) δD values of -57‰ (n = 7, σ = 13‰) and -74‰ (n = 7, σ = 13‰) respectively (collection dates 1982–1989, Friedman et al., 1992). Measured winter precipitation in Owens Valley is more D-depleted (mean October to April = –96‰, n = 6, σ = 15‰) than in Searles Valley due to Rayleigh distillation in rainout over the Sierra Nevada

topographic barrier (~4 km) before reaching Owens Valley. Additionally, moisture can leak south of the mountain range across the Mojave Desert (Friedman et al., 1992) to Searles Valley and become enriched by evaporation during raindrop descent (Friedman et al., 2002). Summer precipitation isotopic compositions reported from Searles Valley (mean, –57‰) and Owens Valley (mean, –62‰) are similar (Friedman et al., 1992). The relative enrichment of summer rainfall could reflect a greater proportion of convective rainfall in summer in addition to the re-evaporation of raindrops as they fall in a hot, low humidity environment (Friedman et al., 1992; Berkelhammer et al., 2012).

1.2. Age Model

Sediment cores SLAPP-SRLS17-1A and 1B (35.7372ºN, 117.33ºW, 495 m asl) were drilled from Searles Lake in 2017 with 95% recovery extending to 78 m below the lake floor (Figure 1b). U/Th dating of evaporite minerals (Stroup et al., in prep) indicate the recovered sediments span 200 ka BP. Stroup et al., (in prep) use 37 U-Th ages to construct a Bayesian age model using BACON (Blaauw & Christeny, 2011). The model considers the mineralogy, stratigraphic superposition, and boundaries between lithological units. To constrain the ages of mud horizons from lower portions of the core lacking salt minerals suitable for dating, a tie point near Termination 2 (T2) was identified, linking the δD_{31alk} record (generated in this study) to the Leviathan composite record $\delta^{18}O_{calcite}$ record, following the approach of Wang et al. (2022). The data were scaled and interpolated before applying a low pass filter to both records to remove high-frequency variability. We then calculated the second derivatives to identify a match point at a gradient of 0. An age constraint of 126.5 ± 0.5 ka from the Leviathan composite record was applied to the feature found at 54.5 m depth in SLAPP-SRLS17-1A. This tie point assumes that changes in the speleothem $\delta^{18}O$ in Nevada and leaf

wax δD in Searles Basin should closely correspond with each other; this assumption is supported by the good agreement between regional speleothem records and Searles basin δD_{wax} over the last 100 ka when the records are anchored by independent U-Th-based age models (section 3.2). Between 200–50 ka, the accumulation rate of lacustrine carbonate muds was 0.2 m/ka (95% CI, ± 3.5 ka). After 50 ka, sediments and salts accumulated more rapidly (1.3 m/ka). The late glacial and deglacial age model is well constrained (± 0.9 ka), but the late Holocene is less well resolved due to slowed deposition after the lake desiccated completely and mining disturbed the upper salts.

2. Material and methods

2.1. Lipid extraction

Lacustrine muds were sampled in 2018 for biomarkers and pollen roughly every 60 cm (~2 ka), avoiding salts that dominate the upper 33 m of the core. We focused on the mud horizons as a test salt sample was found to be barren for plant wax and pollen. As previously described in Peaple et al. (2021), 120 sediment samples (~20 g) were dried, ground, and extracted using a Dionex Accelerated Solvent Extraction system at the University of Southern California with 9:1 dichloromethane (DCM): methanol (MeOH) at 100ºC and 1500 psi to yield the Total Lipid Extract (TLE). The TLEs were separated into neutral and acid fractions using columns backed with NH_2 sepra bulk packing and eluted with 2:1 DCM:isopropanol, followed by 4% HCO_2H in diethyl ether, resulting in neutral and acid fractions, respectively. The neutral fraction was further separated using columns packed with 5% deactivated silica gel, eluting *n*-alkanes with hexanes, and the polar fraction with DCM followed by methanol. *n*-Alkanes were treated with copper to remove elemental sulfur prior to GC analyses. Fatty acids were methylated (to FAMEs) using 95:5 MeOH:hydrochloric acid at 70ºC for 12 h, using MeOH

of known isotopic composition (methyl group $\delta^{13}C$ of –24.7‰ and δD of –187‰).

2.2. GDGT analyses

The neutral polar fraction was analyzed by an Agilent 1260 High-Performance Liquid Chromatography (HPLC) coupled with an Agilent 6120 mass spectrometer at the University of Arizona, following the methods of Hopmans et al. (2016). Compounds were detected in single ion monitoring mode and quantified relative to a C_{46} internal standard. Concentrations of archaeol, caldarchaeol, and the ACE index for salinity were previously reported (Peaple et al., 2021). Here we report concentrations of individual and summed (Σ) isoGDGTs and brGDGTs and calculate temperature, pH, and methane sensitive indicators.

We calculate the branched isoprenoid tetraether (BIT) index:

$$BIT = \frac{Ia+IIa+IIa'+IIIa+IIIa'}{Ia+IIa+IIa'+IIIa+IIIa'+cren} \quad (1)$$

where brGDGTs Ia IIa and IIIa, including both brGDGTs with a methyl group at positions 5 and 6 (5′ and 6′ methyl brGDGTs), are compared with the abundance of crenarchaeol (Hopmans et al., 2004). In lakes, BIT has traditionally been interpreted to represent the balance between soil inputs of brGDGTs and lake production of crenarchaeol (e.g., Verschuren et al., 2009). However, interpretations may differ as bacterial production may dominate in many lakes, and changes in oxycline depth may control the abundance of creanarchaeol-producing Thaumarchaeota (Baxter et al., 2021). As an additional measure of lake stratification, we calculate %GDGT-0 (Sinninghe Damsté, Ossebaar, et al., 2012), which measures the proportion of isoGDGT-0, produced by Thaumarcheota (e.g., Sinninghe Damsté et al., 2012b; Schouten et al., 2013), anaerobic methane-oxidizing archaea (Pancost et al., 2001; Schouten et al., 2001) and methanogenic Euryarchaeota (Schouten et al., 2013, and

190 references therein) relative to crenarchaeol which is produced uniquely by Thaumarchaeota
191 (e.g., Sinninghe Damsté et al., 2002; Schouten et al., 2013):

192 $$\%\mathrm{GDGT}-0=\frac{[GDGT-0]}{[GDGT-0]+[\mathrm{Crenarchaeol}]}\times 100 \quad (2)$$

193 We calculate the CBT′ index (De Jonge et al., 2014) where:

194 $$CBT'=log_{10}\left[\frac{Ic+IIa'+IIb'+IIc'+IIIa'+IIIb'+IIIc'}{Ia+IIa+IIIa}\right] \quad (3)$$

195 CBT′ has been calibrated to pH in east African lakes (Russell et al., 2018):

196 $$pH=7.15-1.59*CBT' \quad (4)$$

197 The temperature-sensitive MBT'_{5Me} index is the relative methylation of the 5′ methyl
198 brGDGTs (De Jonge et al., 2014, Hopmans et al., 2016) and is expressed as:

199 $$MBT'_{5ME}=\frac{(Ia+Ib+Ic)}{(Ia+Ib+Ic+IIa+IIb+IIc+IIIa)} \quad (5)$$

200 where the Type I, II, and III brGDGTs have four, five, and six methyl groups, respectively,
201 and the Type a, b, and c brGDGTs have zero, one, and two rings, respectively. Duplicate
202 analyses and analyses of an internal laboratory standard throughout the runs yielded an error
203 of 0.009 MBT'_{5Me} units (1σ). To convert MBT'_{5Me} to temperature, we use the Bayesian
204 $BayMBT_0$ model, which was generated by calibrating MBT'_{5Me} against the mean temperature
205 of the months above freezing from a global lake dataset (Martínez-Sosa et al., 2021),
206 including lakes over a range of pH (4.3 to 10), salinity (0–275 PSU) and temperature (1.6 to
207 28.1°C).
208 We calculate $IR_{6+7Me,}$ an index sensitive to changes in lake salinity (Huanye Wang et al.,
209 2021):

$$IR_{6+7Me} = \left[\frac{IIa'+IIb'+IIc'+IIIa'+IIIb'+IIIc'}{IIa+IIb+IIc+IIIa+IIIb+IIIc+IIa'+IIb'+IIc'+IIIa'+IIIb'+IIIc'} + \frac{IIIa'''+IIa'''}{IIIa+IIIa'+IIIa'''+IIa+IIa'+IIa'''}\right] \times 0.5 \quad (6)$$

We also calculate TEX_{86} for all samples (Schouten et al., 2002):

$$TEX_{86} = \frac{([GDGT-2]+[GDGT-3]+[cren\prime])}{([GDGT-1]+[GDGT-2]+[GDGT-3]+[cren\prime])} \quad (7)$$

and convert to lake surface temperature (LST) using the calibration (Tierney, Mayes, et al., 2010):

$$LST = TEX_{86} \times 38.874 - 3.4992 \quad (8)$$

in a single sample where BIT <0.3 and %GDGT-0 <50, indicating high thaumarcheotal relative abundance.

2.3. Compound-specific isotopic analyses

n-Alkanoic acids and *n*-alkanes were identified using an Agilent 6890 Gas Chromatograph (GC) connected to an Agilent 5973 MSD mass spectrometer (MS) and quantified by a flame ionization detector (FID). Abundances, average chain length (ACL), and carbon preference index (CPI) were previously reported (Peaple et al., 2021). The carbon and hydrogen isotopic composition of *n*-alkanoic acids ($C_{22\text{-}28}$) and *n*-alkanes ($C_{27\text{-}31}$) were measured for this study using a Thermo Scientific Trace GC equipped with a Rxi®–5 ms column (30 m × 0.25 mm, film thickness 0.25 μm) with a PTV injector in solvent-split mode, coupled via an Isolink combustion/pyrolysis furnace (1000/1400°C) to a Thermo Scientific Delta V Plus isotope ratio mass spectrometer (IRMS) at the University of Southern California. Reference gas linearity was assessed daily across 1–8 V, for $\delta^{13}C$ ($1\sigma = 0.04‰$), and for δD (H_3^+ factor = 10.6 ppm/mV). A standard containing C_{16}-C_{30} *n*-alkanes of known isotopic compositions (A6 mix supplied by A. Schimmelmann, University of Indiana; $\delta^{13}C$ values from –25.9 to –

231 33.7‰ and δD values from –17 to –256‰) was measured daily, allowing for normalization
232 to Vienna Standard Mean Ocean Water (VSMOW) and Vienna Pee Dee Belemnite (VPDB)
233 respectively. Reported $\delta^{13}C$ and δD values for *n*-alkanoic acids were corrected to account for
234 the contribution of the methyl group.

235 **2.4. Palynological Analyses**

236 Pollen assemblages were studied for 113 samples at Syracuse University; for detailed sample
237 processing methodology, see the Supplementary Information. Pollen samples were counted
238 on 400x and 1000x magnification and compared to known pollen keys (Kapp et al., 2000).
239 Our counts found 22 unique taxa, though samples were dominated by *Pinus* pollen (e.g.,
240 greater than 40% of each sample). Pollen assemblages are expressed in percentages and
241 pollen influx rates (grains/cm^2/yr). The similarity of the broad trends across these two ways
242 of expressing the pollen data increases our confidence that the patterns in our data are robust.
243 For our analysis, we exclude one sample at 27.49 m associated with a tephra layer. To
244 identify the patterns of variability in the pollen data, we calculated the Bray-Curtis
245 dissimilarity index between samples, using pollen taxa that were present in 2 or more samples
246 at a percentage greater than 2%. This index calculates the compositional dissimilarity
247 between two ecological samples in space or time and minimizes the contribution of rare taxa
248 to the dissimilarity between samples (Faith et al., 1987). We used a matrix of pairwise Bray-
249 Curtis indices between samples to perform a non-metric multidimensional scaling (NMDS).
250 NMDS iteratively moves all samples in 2-dimensional ordination space so that their final
251 distance from each pairwise sample is proportional to the Bray-Curtis dissimilarity between
252 those two samples. It is analogous to principle components analysis in that the distance
253 between samples on the plot provides a guide to their dissimilarity but is more robust for
254 assemblages containing rare taxa (Faith et al., 1987; Fasham, 1977). The results from this

NMDS analysis are used to guide our interpretation of specific plant taxa in the pollen record.

2.5. Correlation analysis

All correlations between time series use non-parametric methods that account for serial correlation (Ebisuzaki, 1997).

3. Results and Discussion

3.1. Vegetation reconstructions from Searles Lake spanning 200 kyr

3.1.1. Pollen

We present a multi-proxy biomarker and pollen study of vegetation change as recovered from the sediments of Searles Lake in the SLAPP-SRLS17 sediment core. All vegetation-related data obtained from the core are shown in stratigraphic context (Figure S4) and on the age scale (Figure 2). Because of their long-distance dispersal and high productivity, Searles pollen is dominated by *Pinus* spp (Figure 2) (Campbell et al., 1999; Wood, 2000). It has been theorized that during glacials, pines likely expanded into the lowlands while being restricted in the uplands (Litwin et al., 1999; Woolfenden, 2003). However, pollen from other taxa is more diagnostic of vegetation change. During cooler/wetter glacial periods, Taxodiaceae-Cupressaceae-Taxaceae (TCT), mostly *Juniperus* spp, increase in Searles sediments. Glacial increases in *Juniperus*-type pollen have previously been reported from sediment cores from the Gulf of California to the Great Basin (Byrne, 1982; Davis, 1998) and in packrat middens across southwestern North America (Koehler et al., 2005; Thompson & Anderson, 2000). Middens in the Central Mojave identify the local expansion of drought-sensitive *J. osteosperma* during glacials indicating moist conditions in the lowlands (Holmgren et al., 2010; Koehler et al., 2005; Willson et al., 2008).

During interglacials, herbaceous taxa like Asteraceae and Amaranthaceae increased (Figure 2a). We sum Asteraceae and Amaranthaceae together to represent desert shrubs. NMDS analysis reveals that glacial and interglacial samples from Searles lake show distinct pollen assemblages and that these changes are primarily driven by changing proportions of desert shrub and *Juniperus*-type pollen (Figure S4). Desert shrub proportions were previously modeled by machine learning on *n*-alkane and *n*-alkanoic acid homologs in the same sediments (Peaple et al., 2021; Figure 2b), and the comparison with desert shrubs reconstructed by pollen (Figure 2c) indicates similar long-term trends when high-frequency changes are removed ($r = 0.42$, $p>0.01$). Pollen reveal the taxa present but are not necessarily expected to be proportional to inputs of plant wax given differences in pollen productivity (wind vs. insect-pollinated) and leaf waxiness, along with different release and transport mechanisms. For example, although *Juniperus* spp. pollen are abundant in glacials, we do not find their modal C_{33} *n*-alkanes (Diefendorf et al., 2015) to be abundant in Searles Lake sediments suggesting lower proportional wax productivity or transport compared to their pollen.

Pollen and biomarkers were linearly interpolated onto 2 kyr sampling resolution to assess shared variance by principal component analysis (PCA; Figure 3). The PCA analysis identifies a negative relationship between dominant *Pinus spp* pollen and TCT (mostly *Juniperus* spp.). *Juniperus* spp. is associated with Artemisia, denoting their glacial co-occurrence (Figures 2 and 3). The ACE salinity index and desert taxa *Amaranthaceae* show a correspondence, similar to their presence in salty lowland areas today. Desert shrub pollen increases with warming, consistent with prior reports (Lyle et al., 2010).

3.1.2. Plant wax $\delta^{13}C$ and δD

Carbon and hydrogen isotope evidence from long-chain plant wax biomarkers reveals additional information about vegetation. We consider the long chain *n*-alkanoic acids (C_{28acid}) and *n*-alkanes (C_{31alk}) (Figure 3), commonly used to reconstruct paleoenvironmental information (e.g., Feakins and Sessions, 2010; Feakins et al., 2019; Tierney et al., 2010). In this study, the correlation between the two compound classes are weak suggesting distinct sourcing (C_{28acid} and C_{31alk} correlations are not significant for δD and $r = 0.4$, $p<0.05$ for $\delta^{13}C$). Macrophytes have been identified as a possible confounding input based on machine learning on chain length distributions (Peaple et al., 2021). For the *n*-alkanoic acids, a positive correlation between ACE (lake salinity) and δD_{26acid} ($r = 0.4$, $p < 0.05$) and correlations between C_{28acid} and C_{26acid} ($r = 0.4$ and 0.6, $p<0.05$) for δD and $\delta^{13}C$ respectively), suggests that the C_{28acid} may include aquatic sources. We therefore rely on the C_{31alk} as a proxy for terrestrial vegetation in this study.

Supporting their terrestrial plant origins, we find agreement between $\delta^{13}C_{31alk}$ and pollen, with $\delta^{13}C_{31alk}$ increasing with higher Amaranthaceae (C_4 and C_3 members) pollen percentages and influx rates (Figures 2d, 3, and Figure S4), suggesting that the C_4 components are shrubs. In contrast, grasses are nearly absent from the pollen record during interglacial intervals, making it unlikely that the $\delta^{13}C_{31alk}$ signal reflects C_4 grasses (Figure 2d). The C_4 pathway is used in some woody, halophilic desert plants sampled in the catchment today, including plants in the *Atriplex* and *Suaeda* genera (see Supplementary Information). These plants are phreatophytes and thrive in locations with shallow groundwater (Patten et al., 2008). C_3 plants in the catchment include conifers, some of which (*Juniperus* spp.) produce long-chain *n*-alkanes (Peaple et al., 2021).

The *n*-alkanes yield a clear D-depleted glacial and D-enriched interglacial pattern (Figure 2e).

323 δD_{31alk} has a close phasing with desert shrub pollen (sum of *Amaranthaceae* and *Asteraceae*)
324 and temperature (Figures 2c and 3), and this covariation of proxies suggests a common driver
325 which will be explored when compared to regional and global climate (in Section 4.2).
326 During arid climates, like today, we assume that desert shrubs dominate the *n*-alkane record.
327 Although the details are necessarily unconstrained for past pluvial climates in southern
328 California, trees in modern temperate North American forests and woodlands are prolific
329 producers of *n*-alkanes. They have been shown to contribute strongly to lakes rather than
330 marginal plants (Freimuth et al., 2019). We thus infer that plant wax *n*-alkanes may have
331 been supplied by wind/fluvial transport to Searles Lake from catchment woody shrubs and
332 trees under pluvial conditions. We reconstruct δD_{precip} using the constant local fractionation
333 by plants ($\varepsilon_{31alk/p,}$ -93‰), determined from regional calibration across the modern aridity
334 gradient (Feakins and Sessions, 2010). Sensitivity tests that assess the effect of changing
335 vegetation based on pollen and plant wax $\delta^{13}C$ (see Supplementary Information, Figure S2)
336 lead to confidence in the constant fractionation and hydroclimate interpretations here.

337 **3.2. Plant wax evidence for glacially paced changes in hydroclimate**

338 The Searles Lake δD_{31alk} record (Figure 4) is dominated by glacial to interglacial variability,
339 with interglacials characterized by more positive values and glacials by more negative values.
340 After accounting for the ice volume corrections for seawater δD, and the apparent
341 fractionation by plants, we can interpret plant wax δD_{31alk} as precipitation isotopic variations
342 (Figure 4c, see Supplemental Information for method details). δD_{precip} averages -93‰ (σ =
343 6‰, n = 9) during interglacials and -125‰ (σ = 8‰, n = 9) during glacials. The Searles
344 δD_{precip} closely matches global climate records of glacial to interglacial changes in pCO_2
345 (Figure 4b), ice volume, and deep ocean temperature changes interpreted from benthic

foraminiferal oxygen isotopes (Figure 4c) across two glacial-interglacial cycles.

Climate model experiments support theoretical expectations of D-depletion associated with moisture condensation at colder temperatures and as ice versus liquid cloud droplets, as expected in a glacial climate (Jasechko et al., 2015). Additionally, the southerly movement of storm tracks would introduce more winter-season D-depleted North Pacific sourced precipitation (Oster et al., 2015; Tabor et al., 2021) and a decrease in D-enriched North American Monsoon summer rainfall (Bhattacharya et al., 2018) (see section 3.4.3 for more details).

Comparison of the two glacial cycles in Searles Lake records suggests that the penultimate glacial maximum (PGM) was cooler and wetter compared to the last glacial maximum (LGM), which is in contrast to records of global climate change that show similar magnitudes of changes during both glacial maxima (Figure 4). The δD_{precip} is lower (Figure 4c), the $BayMBT_0$ temperature is 5ºC lower (Figure 4d), and shrub pollen reaches a 200 ky minimum (Figure 4e) during the later stages of the penultimate glaciation compared to the LGM. The glacial-interglacial variations at Searles Lake are captured by changes in three independent, climate-sensitive proxies: plant wax, bacterial membrane lipids, and pollen microfossils. The climate changes that produce variations in these proxies are explored and evaluated further, in discussions of regional precipitation archives (Section 4.3), past water availability (Section 4.4), and past temperatures (Section 4.5).

3.3. Comparison with regional precipitation isotope archives

We compare the new 200 kyr Searles Lake plant wax reconstruction of δD_{precip} to regional speleothem $\delta^{18}O_{calcite}$ records from Devils Hole (Moseley et al., 2016; Winograd et al., 1992) and the Leviathan. Pinnacle and Lehman caves composite (Lachniet et al., 2014). The cave

and plant wax records show similar glacial to interglacial pacing (Figure 5), with higher $\delta^{18}O$ and δD values during interglacials and lower values during glacials. Spectral analyses of each record (Figure 5e–g) show that Searles Lake and Devils Hole are paced by obliquity, whereas the Leviathan composite is paced additionally by precession. For the obliquity response, summer insolation maxima correspond to higher $\delta^{18}O$ and δD, and the magnitude of change can be compared after accounting for the mass-dependent fractionation scaling of 8 (Figure 5h). The amplitude of variability at Devils Hole, less than half that of Leviathan, was attributed to aquifer averaging (Lachniet et al., 2017) and the slow rate of carbonate deposition (Moseley et al., 2016). In addition, cave temperature can modulate the amplitude of $\delta^{18}O_{calcite}$ through its control on equilibrium fractionation between water and calcite (Hendy, 1971; Kim & O'Neil, 1997). Studies of triple oxygen isotopes have shown sensitivity to mineralization temperature at Leviathan and evaporation at Lehman (Huth et al., 2022). We apply a 6–10°C cooling (consistent with our temperature reconstruction) during glacials to interpretation of $\delta^{18}O_{calcite}$ in the Leviathan composite record (black bar Figure 5h). In contrast, clumped isotope methods suggested Devils Hole remained within ±1°C over the past 600 kyrs because of the large aquifer size (Bajnai et al., 2021).

The correspondence of the glacial-interglacial changes and obliquity pacing with an independent proxy, such as plant wax in lake sediments, provides independent corroboration of the importance of obliquity pacing on large-scale hydroclimate and atmospheric circulation. We note that obliquity and eccentricity are the dominant components of North American ice volume (Bintanja & Van De Wal, 2008). As such, changes in ice-sheet extent may have been a forcing of hydroclimate with glacial-interglacial and obliquity signals recorded in both the Searles Lake and Devils Hole precipitation isotope archives. The precessional swings in the Leviathan composite $\delta^{18}O$ record may reflect cave air temperature

changes that affect calcite fractionation. Plant wax δD_{precip} is not considered temperature sensitive, but carries uncertainty associated with fractionation, aridity, and plant type. The similarity between the plant wax and cave records supports the obliquity pacing of precipitation isotopes, but their climate significance is less clear. Although precipitation isotopes are valued hydrological tracers that capture the obliquity pacing and glacial-interglacial climate, they remain an indirect proxy for moisture availability on the landscape, leaving a need for additional proxy constraints on hydroclimate.

3.4. Searles Lake salinity and regional moisture availability

3.4.1. Salinity proxies

Salinity inversely covaries with lake depth in terminal lakes (Olson & Lowenstein, 2021). We compare results from two biomarker indices purportedly responsive to lake salinity, the archaeal-derived ACE index (Figure 6a) previously reported in Peaple et al. (2021), and the bacterial-derived IR_{6+7me} (Figure 6b) tested here for its potential to differentiate freshwater conditions. While the ACE index (Turich and Freeman, 2011) is sensitive to lake hypersalinity (Wang et al., 2013), it loses sensitivity below 60 PSU (He et al., 2020). In contrast, the IR_{6+7me} index was found to have sensitivity below 100 PSU (He et al., 2020). We compare both approaches in Searles Lake sediments. ACE values range from 0 to 100, and IR_{6+7me} range from 0.4 to 0.8. ACE appears to perform well in comparison to lithology: low ACE values were found in thick muds (76–50 m, 29–28 m and 25–22 m) interpreted as perennial, deep lake deposits, whereas high ACE occurred in interbedded muds and salts (36–34 m) including trona and burkeite associated with hypersaline conditions (Olson and Lowenstein, 2021; Olson et al., in review). Downcore we find a moderate positive correlation between ACE and IR_{6+7me} in muds between 76 and 50 m ($r = 0.43$, $p < 0.01$) suggesting both

proxies are performing well in perennial, saline conditions. No significant correlation exists in the interbedded muds and salts deposited in saline to hypersaline conditions. We find IR_{6+7me} (0.60) is lower (i.e. fresher) in hypersaline lake stages than in deeper lake mud units (0.66) indicating that this proxy fails at high salinities and needs joint application with ACE for verification, or should not be applied when there are bedded evaporites. However, IR_{6+7me} index confirms expectations of being sensitive at low salinity as it detects the lowest IR_{6+7me} values (freshest waters) between 140–130 ka. ACE is low between 140-130 ka, but there are several other periods with similarly low ACE in the Searles Lake record (Figure 6a), suggesting that ACE is less sensitive than IR_{6+7me} for differentiating amongst the freshest conditions of the 200 kyr record. Thus we recommend dual application of these salinity proxies, to reconstruct salinity, with IR_{6+7me} utility limited to low salinity settings. We conclude that a terminal lake with varying salinity was the normal state for Searles Lake across most of 200 kyr, with brief interludes of freshwater conditions with possible throughflow.

The Searles Lake ACE (Figure 6a) and IR_{6+7me} (Figure 6b) records share key similarities with the Devils Hole water table reconstructions (Wendt et al., 2018) (Figure 6d): a more saline lake corresponds to low water table during the previous interglacial (Eemian), and a fresher lake accompanies high water tables during Heinrich 11 and 1. The mean ACE and IR_{6+7me} were 19% lower and 1% lower, respectively, during MIS 6 relative to MIS 2 Searles Lake. Similarly Devils Hole calcite deposits are much thicker in MIS 6 suggesting longer and more frequent water table highstands compared to MIS 2.

3.4.2. Lake overturning and outflow

We find additional biomarker evidence suggesting unique limnological conditions existed in

Searles Lake between 140–130 ka during late MIS 6. In comparison to high BIT and %GDGT-0 indexes (~1 and >99%, respectively) in most of the 200 kyr record, indicating stratified low productivity lakes, both indices decrease to medians of 0.72 and 46%, respectively, between 140–130 ka (Figure 6c), and IR_{6+7me} values reach a freshwater minimum. Modern studies suggest that crenarchaeol-producing Thaumarchaeota live above a shallow oxycline (Baxter et al., 2021; Schouten et al., 2012; Wang et al., 2019), and methanogenic archaea, which produce GDGT-0, occur below the oxycline of an anoxic lake (Baxter et al., 2021; Bechtel et al., 2010; Wang et al., 2019). Searles Lake sediments typically have low crenarchaeol relative to brGDGTs (high BIT) and GDGT-0 (high %GDGT-0), suggesting salinity stratified and/or low oxygen conditions. But from 140–130 ka these biomarkers denote freshwater, high lake productivity, and a vigorously mixed water column with deep oxygenation. Lake overturning is enabled in freshwater systems where winter cooling causes surface waters to sink, also assisted by the turbulence of water inflow and outflow (Rimmer et al., 2011). While much of SLAPP-SLRS17 consists of dolomite and less common laminated aragonite thought to reflect salinity-stratified conditions, this portion of the core is characterized by massive carbonate-free mud (Figure S5). These massive mud deposits may reflect well-mixed lake conditions that allowed for bioturbation.

Searles Lake was likely briefly overflowing during MIS 2, likely associated with relatively low ACE and IR_{6+7me} between 20 – 17 ka. However, we do not see a decrease in BIT or %GDGT-0 during MIS 2, suggesting that the lake was not well oxygenated. Minimum ACE and IR_{6+7me} were lower during late MIS 6 than in MIS 2, indicating lower minimum water salinity during MIS 6. Together with evidence for lack of overspill into downstream Lake Panamint, this suggests that Searles was not vigorously outflowing for any extended period during MIS 2. Additionally, constant sediment deposition on the lake floor from MIS 6 to the

present has reduced the lake volume necessary to reach the sill elevation. The lake depth required for spillover was 274 m in MIS 6, but only 225 m during MIS 2 to (Smith, 2009). Given that Searles Lake was vigorously outflowing during late MIS 6 with 45 m deeper water levels, we infer greater inflow and a wetter climate state than during MIS 2.

Searles Lake shoreline deposits indicate brief episodes of outflow occurred between 15–12 kyr (Lin et al., 1998; Smith, 2009), resulting in an 180–200 m deep lake being present in Panamint Valley during periods of MIS 2 (Jayko et al., 2008). During MIS 6, Searles Lake shoreline deposits (Smith, 2009) and chlorine transfer budget (Jannik et al., 1991) suggest a period of intensive overflow into Panamint Valley, which resulted in the formation of a >300 m deep Lake Panamint which overspilled into Lake Manly in Death Valley (Jayko et al., 2008). This overspill resulted in Lake Manly being deeper during MIS 6 than MIS 2 (Forester et al., 2005; Roberts & Spencer, 1998). Further upstream, dates of lake highstands and outflows suggest that Mono Lake was possibly overspilling into the Owens River catchment during MIS 6 but not during MIS 2 (Reheis et al., 2002; Reheis pers. comm., 1/20/2022). The biomarker evidence provides a new way to detect lake flushing associated with pluvials.

3.4.3. Heinrich Stadials 11 and 1

We now consider the climate dynamics behind these pluvials. Benthic $\delta^{18}O$ values (Lisiecki & Raymo, 2005) and atmospheric pCO_2 (Lüthi et al., 2008) are broadly similar in amplitude during the last two glacial cycles (Figure 4a, b). However, the PGM has a longer duration than the LGM (Jouzel et al., 1993), manifested regionally by the prolonged high water table at Devils Hole (Wendt et al., 2018). However at Searles Lake, the freshest and highest lake levels are reconstructed not during the PGM but H11 during Termination 2, and this was wetter than H1 during Termination 1. Coastal pollen records from central California marine

core ODP Site 1018 corroborate this pluvial comparison, finding a 20% greater decrease in shrub pollen associated with the T2 extreme wet event than the T1 pluvial (Lyle et al., 2010). The T2 pluvial is wetter than all other glacial terminations of the past 600 kyrs as recorded by the longer records from ODP Site 1018 pollen and by the Searles to Panamint chlorine transfer budget (Jannik et al., 1991).

Globally T2 and 1 differ in their sea-level rise, T2 being a continuous, rapid rise, whereas T1 has a two-step rise (Clark et al., 2020). T2 also had stronger insolation forcing during the Northern Hemisphere summer solstice (Bova et al., 2021). While Sierra Nevada glacial melt could be a transient contributor at terminations, extended wet conditions require increased precipitation. Tracers of cave infiltration, including trace element ratios, Sr/Ca, $^{87}Sr/^{86}Sr$ and carbon isotopic evidence from Lehman Cave, Nevada, also suggest that H11 was wetter than the preceding MIS 6 glacial maximum and terminated rapidly within 2 kyrs (Cross et al., 2015). The disconnect between P–E and $\delta^{18}O_{calcite}$ identified in Lehman Cave (Cross et al., 2015), matches the lack of significant correlation we observed between the Searles Lake δD_{precip} with Searles Lake salinity proxies. This disconnect could indicate separation of timing of local temperature change and that of large-scale hydroclimate dynamics (Cross et al., 2015).

Model simulations link North Atlantic cooling during Heinrich stadials to pluvials in southwestern North America (McGee et al., 2018). Proxy records suggest freshwater inputs to the North Atlantic slow the Atlantic Meridional Overturning Circulation, leading to winter cooling in the Northern Hemisphere, causing the Inter-Tropical Convergence Zone to shift southward (Jacobel et al., 2016), and that southward migration is greater in T2 than in T1 (Jacobel et al., 2017), consistent with the deeper lake at Searles in T2 compared to T1. These

509 dynamical changes intensify the northern Hadley Cell, accelerating the subtropical jet and
510 increasing the winter season delivery of atmospheric river precipitation to southwestern
511 North America (McGee et al., 2018). Precipitation from tropical/sub-tropical atmospheric
512 rivers is relatively enriched in the heavier isotopes of D and ^{18}O compared to North Pacific-
513 derived moisture (Berkelhammer et al., 2012). Thus, the increase in δD_{precip} we observe at
514 Searles Lake and the increase in $\delta^{18}O_{calcite}$ seen in Lehman Cave (Cross et al., 2015) during
515 terminations are consistent with these ocean-atmosphere dynamics. Temperature changes
516 likely play a secondary role in amplifying the δD_{precip} signal (Dansgaard, 1964).

517 3.4.4. Timing of the T2 pluvial

518 Regarding the timing of the pluvial close to H11, we note the implications of the age model
519 selection represented in the comparison in Figure 6. The SLAPP-SRLS17 preferred age
520 model based on U/Th incorporates an age tie point between the Leviathan composite
521 $\delta^{18}O_{calcite}$ and Searles Lake δD of C_{31} alkane, with an age of 126.5 kyr, at a gap in the U/Th
522 constraints (Section 1.2). This age model places the peak of the vigorous overflow event in
523 Searles Valley (Figure 6a, b, c, d, and e) at 131.4 kyr, coinciding with H11 (Cross et al.,
524 2015). Without the tie point, the U/Th-only age model places the overflow event later at
525 126.6 kyr. Regional climate records from southwestern North America uniformly suggest that
526 MIS 5e was relatively dry (e.g., Litwin et al., 1999; Woolfenden, 2003; Cross et al., 2015;
527 Wendt et al., 2018). Based on the assumption that the tie point to regional cave records is
528 appropriate, the microbial lipid record from the Searles Basin supports wet conditions during
529 H11 followed by a shift to drier conditions at the beginning of MIS 5.

530 **3.5. Terrestrial temperatures**

531 We contribute to sparse evidence for terrestrial temperature change on land with the new

biomarker records from Searles Lake (Figure 7). We reconstruct the mean annual temperature of months above freezing (Figure 7a) of Searles Lake using the $BayMBT_0$ calibration of the bacterial lipid MBT'_{5Me} index in global lakes (Martínez-Sosa et al., 2021). This record overlaps with the 33–9 kyr record from Lake Elsinore with the same proxy (Feakins et al., 2019), recalibrated with the same MAF (mean months above freezing) calibration here (Figure 7a). Both lakes show 10˚C glacial-to-Holocene warming and similar magnitude variability within glacials, with notably warm intervals from 50–30 kyrs at Searles (22°C, with a calibration uncertainty, RMSE of 3°C), corroborating reports of warm times during the last glacial in the region (Feakins et al., 2019).

While brGDGT reconstructions can suffer from biases induced by shallow lake depth, hypersalinity (He et al., 2020), and high alkalinity (Martínez-Sosa et al., 2021) in part related to more influence from allochthonous inputs from soil-derived brGDGTs in less productive, saline lakes (Martínez-Sosa et al., 2021), our tests corroborate the use of the $BayMBT_0$ lake calibration (see Supplemental Information, Figures S8-10). Briefly, Searles Lake brGDGT abundance distributions are more similar to global lakes (Martínez-Sosa et al., 2021) than soils (Dearing Crampton-Flood et al., 2020). We also note that reconstructed temperatures from Searles Lake and Lake Elsinore during the Holocene are similar to modern measured MAF. Independent corroboration of the magnitude of the terrestrial deglacial warming comes from noble gas groundwater paleotemperature reconstructions from the Mojave Desert (Kulongoski et al., 2009) and San Diego (Seltzer et al., 2021) that capture evidence for 7–10°C deglacial warming (Figure 7b).

In the 200 kyr $BayMBT_0$ record from Searles Lake, we identify the penultimate glacial as colder than the last glacial. That cooling occurred between 215–150 kyr, followed by sharp

555 warming during T2 (140–130 kyr) and relative temperature stability between 130–50 kyr,
556 pronounced cooling from 50–18 kyr, and then deglacial warming, as previously described.
557 Within the low BIT interlude (BIT = 0.3) of the penultimate glaciation at 131.4 kyr, we were
558 able to obtain a single archaeal, isoGDGT-based TEX_{86} estimate of lake surface temperature
559 applying the lake calibration (Tierney, et al., 2010) to one sample yielding an estimate of 12
560 ± 2°C (Figure 7a). This sample also yielded a $BayMBT_0$ temperature estimate of 14 ± 3°C,
561 equivalent within calibration uncertainties. We note that the coldest temperatures are also
562 associated with the freshest conditions in the lake (low ACE, lowest IR_{6+7me}) and the
563 indication of overflow into Panamint based on the %GDGT-0 and BIT. Overturning in lakes
564 increases brGDGT production and export to sediments (Loomis et al., 2014), which could
565 result in a larger proportion of lake-derived bGDGT compared to allochthonous inputs. Given
566 that soil calibration of MBT'_{5Me} underestimates temperatures when applied to lakes
567 (Martínez-Sosa et al., 2021), a decreased input of soil-derived brGDGTs could lead to a
568 decrease in reconstructed temperatures independent of a change in air temperature.
569 Additionally, this period is associated with a significant increase in CBT' (decrease in pH)
570 which could alter the bacterial community and may influence the temperature response (De
571 Jonge et al., 2021). MBT'_{5Me} can show lake depth dependency in shallow, alpine freshwater
572 lakes (Stefanescu et al., 2021; Weber et al., 2018) which could result in deeper lakes being
573 biased to cooler temperatures. However, lake depth is not related to MBT'_{5Me} in global
574 lacustrine brGDGTs compilations (Martínez-Sosa et al., 2021), and we no find no correlation
575 between ACE and MBT'_{5Me} ($r = 0$, $p > 0.05$) here which suggests that changes in salinity (lake
576 depth) are not a dominant driver of MBT'_{5Me} in saline to hypersaline Searles Lake.

577 During the glacials terrestrial temperature changes by 10°C between 50–30 ka (Figure 7a),

indicating significant terrestrial temperature variability. In contrast glacial-interglacial pacing dominates the SSTs (Figure 7c), with a smaller amplitude (5°C) compared to the terrestrial records and minimal variability within glacials. Shrub pollen (Figure 7c) has a moderate correlation with brGDGT reconstructed terrestrial temperatures (Figure 7a, $r = 0.44$, $p<0.05$) suggesting that temperature is a dominant driver of vegetation cover in the drought-stressed region. This indicates the importance of terrestrial temperature reconstructions to understand the relationships between temperature, moisture balance and vegetation, with lessons for future warming.

4. Conclusions

We present a new biomarker and pollen record from the SLAPP core drilled in Searles Lake spanning the past 200 kyr. We show evidence from pollen and plant wax for vegetation change and find that shrub pollen responds to glacial-interglacial temperature change. We show that the plant wax *n*-alkane-based proxy for δD_{precip} is characterized by large glacial to interglacial and obliquity changes, likely driven by variations in ice volume. There is a strong correlation ($r = 0.79$, $p > 0.01$) determined by non-parametric methods that account for serial correlation (Ebisuzaki, 1997) between changes in δD_{precip} and changes in $\delta^{18}O_{calcite}$ from the nearby Devils Hole speleothem. The similar pacing suggests that both archives are recording precipitation isotopic composition; however, the Searles Lake δD_{precip} record shows larger amplitude changes.

We also present more direct indicators of moisture availability. The ACE index of lake salinity and IR_{6+7me} are consistent with lake core lithology and shoreline markers. We find similarities between Devils Hole water table and regional lake depths, with pluvials during glacials and drier interglacial conditions. However, we find that Searles Lake was likely

deeper during the penultimate glacial, MIS 6, compared to MIS 2, with the wettest conditions occurring during Termination 2, especially Heinrich stadial 11. During H11, Searles Lake was well-mixed and overflowed into Panamint Basin, interpreted from the large decrease in BIT and %GDGT-0. In comparison, Searles Lake remained a stratified, saline, terminal lake during the last lake highstand in H1.

Both brGDGT-derived temperatures and the proportion of shrub pollen increase during interglacial periods, although glacial temperature minima differ, with terminal MIS 6 being 4°C cooler than MIS 2. We find less shrub pollen, a fresher lake, and more D-depleted precipitation in the T2 pluvial, providing confidence that the T2 pluvial was wetter than the T1 pluvial from these independent lines of evidence from the sediments in the Searles Lake core. This 200 kyr record reveals differences between the two glacial pluvials and between two interglacials, highlighting the sensitivity of southwestern North America's hydroclimate.

Acknowledgments

The plant wax study and GRA (Peaple) were supported by U.S. National Science Foundation Grant NSF-EAR-1903665 to S.F., GDGT analyses were supported by the Packard Fellowship for Science and Engineering to J.T., and the pollen analyses were supported by a sub-award to T.B. from NSF-EAR-1903659 to T.L. Drilling was supported by the Comer Science and Education Foundation Grant to D.M. and T.L. We thank Searles Valley Minerals for access and Jade Zimmermann in particular. The sample material used in this project was provided by the Continental Scientific Drilling Facility, University of Minnesota. We thank the SLAPP team involved in coring and collaborative discussions of surroundings and paleoenvironment, as well as Marith Reheis for discussion of Lake Russell overflow, Jay Quade for plant identification in the Mojave Desert, Alan Juarez for field assistance in the San Bernardino Mountains, and Patrick Murphy for assistance measuring GDGTs. Thanks to the Associate Editor Carlos Jaramillo and two anonymous reviewers.

Author contributions**:** SF, DM and TL designed the study and acquired the funding; MP

conducted the biomarker analyses, graphed the data and wrote the paper; SF supervised MP and contributed to writing; TB conducted pollen analyses and contributed to writing; JT supported GDGT analyses; KO contributed sediment stratigraphy; JS contributed the age model; all authors contributed.

Conflict of Interest

The authors declare no financial conflicts of interests for any author or their affiliations.

Data Availability Statement

Data files are archived at the NOAA paleoclimatology database at

https://www.ncei.noaa.gov/access/paleo-search/study/36393

Supporting Information

Supporting information may be found in the online version of this article.

References

Bacon, S. N., Jayko, A. S., Owen, L. A., Lindvall, S. C., Rhodes, E. J., Schumer, R. A., & Decker, D. L. (2020). A 50,000-year record of lake-level variations and overflow from Owens Lake, eastern California, USA. *Quaternary Science Reviews*, *238*, 106312. https://doi.org/10.1016/j.quascirev.2020.106312

Bajnai, D., Coplen, T. B., Methner, K., Löffler, N., Krsnik, E., & Fiebig, J. (2021). Devils Hole Calcite Was Precipitated at ±1°C Stable Aquifer Temperatures During the Last Half Million Years. *Geophysical Research Letters*, *48*(11). https://doi.org/10.1029/2021GL093257

Baxter, A. J., van Bree, L. G. J., Peterse, F., Hopmans, E. C., Villanueva, L., Verschuren, D., & Sinninghe Damsté, J. S. (2021). Seasonal and multi-annual variation in the abundance of isoprenoid GDGT membrane lipids and their producers in the water column of a meromictic equatorial crater lake (Lake Chala, East Africa). *Quaternary Science Reviews*, *273*, 107263. https://doi.org/10.1016/J.QUASCIREV.2021.107263

Bechtel, A., Smittenberg, R. H., Bernasconi, S. M., & Schubert, C. J. (2010). Distribution of branched and isoprenoid tetraether lipids in an oligotrophic and a eutrophic Swiss lake: Insights into sources and GDGT-based proxies. https://doi.org/10.1016/j.orggeochem.2010.04.022

Berkelhammer, M., Stott, L., Yoshimura, K., Johnson, K., & Sinha, A. (2012). Synoptic and mesoscale controls on the isotopic composition of precipitation in the western United States. *Climate Dynamics*, *38*(3–4), 433–454. https://doi.org/10.1007/s00382-011-1262-3

Bhattacharya, T., Tierney, J. E., Addison, J. A., & Murray, J. W. (2018). Ice-sheet

661 modulation of deglacial North American monsoon intensification. *Nature Geoscience*, 1.
662 https://doi.org/10.1038/s41561-018-0220-7
663 Bintanja, R., & Van De Wal, R. S. W. (2008). North American ice-sheet dynamics and the
664 onset of 100,000-year glacial cycles. *Nature 2008 454:7206*, *454*(7206), 869–872.
665 https://doi.org/10.1038/nature07158
666 Bischoff, J. L., & Cummins, K. (2001). Wisconsin Glaciation of the Sierra Nevada (79,000-
667 15,000 yr B.P.) as recorded by rock flour in sediments of Owens Lake, California.
668 *Quaternary Research*, *55*(1), 14–24. https://doi.org/10.1006/qres.2000.2183
669 Blaauw, M., & Christeny, J. A. (2011). Flexible paleoclimate age-depth models using an
670 autoregressive gamma process. *Bayesian Analysis*, *6*(3), 457–474.
671 https://doi.org/10.1214/11-BA618
672 Bova, S., Rosenthal, Y., Liu, Z., Godad, S. P., & Yan, M. (2021). Seasonal origin of the
673 thermal maxima at the Holocene and the last interglacial. *Nature 2021 589:7843*,
674 *589*(7843), 548–553. https://doi.org/10.1038/s41586-020-03155-x
675 Byrne, R. (1982). Preliminary pollen analysis of Deep Sea Drilling Project Leg 64 Hole 480
676 (Cores 1-11).
677 Campbell, I. D., McDonald, K., Flannigan, M. D., & Kringayark, J. (1999). Long-distance
678 transport of pollen into the Arctic. *Nature*, *398*(6731), 29–30.
679 https://doi.org/10.1038/19891
680 Clark, P. U., He, F., Golledge, N. R., Mitrovica, J. X., Dutton, A., Hoffman, J. S., & Dendy,
681 S. (2020). Oceanic forcing of penultimate deglacial and last interglacial sea-level rise.
682 *Nature 2020 577:7792*, *577*(7792), 660–664. https://doi.org/10.1038/s41586-020-1931-
683 7
684 Cross, M., McGee, D., Broecker, W. S., Quade, J., Shakun, J. D., Cheng, H., et al. (2015).
685 Great Basin hydrology, paleoclimate, and connections with the North Atlantic: A
686 speleothem stable isotope and trace element record from Lehman Caves, NV.
687 *Quaternary Science Reviews*, *127*, 186–198.
688 https://doi.org/10.1016/J.QUASCIREV.2015.06.016
689 Dansgaard, W. (1964). Stable isotopes in precipitation. *Tellus*, *16*(4), 436–468.
690 https://doi.org/10.1111/j.2153-3490.1964.tb00181.x
691 Davis, O. K. (1998). Palynological evidence for vegetation cycles in a 1.5 million year pollen
692 record from the Great Salt Lake, Utah, USA. *Palaeogeography, Palaeoclimatology,*
693 *Palaeoecology*, *138*(1–4), 175–185. https://doi.org/10.1016/S0031-0182(97)00105-3
694 Dearing Crampton-Flood, E., Tierney, J. E., Peterse, F., Kirkels, F. M. S. A., & Sinninghe
695 Damsté, J. S. (2020). BayMBT: A Bayesian calibration model for branched glycerol
696 dialkyl glycerol tetraethers in soils and peats. *Geochimica et Cosmochimica Acta*, *268*,
697 142–159. https://doi.org/10.1016/j.gca.2019.09.043
698 Diefendorf, A. F., Leslie, A. B., & Wing, S. L. (2015). Leaf wax composition and carbon
699 isotopes vary among major conifer groups. *Geochimica et Cosmochimica Acta*, *170*,
700 145–156. https://doi.org/10.1016/j.gca.2015.08.018
701 Ebisuzaki, W. (1997). A method to estimate the statistical significance of a correlation when
702 the data are serially correlated. *Journal of Climate*, *10*(9), 2147–2153.
703 https://doi.org/10.1175/1520-0442(1997)010<2147:AMTETS>2.0.CO;2
704 Faith, D. P., Minchin, P. R., & Belbin, L. (1987). Compositional dissimilarity as a robust
705 measure of ecological distance. *Vegetatio 1987 69:1*, *69*(1), 57–68.
706 https://doi.org/10.1007/BF00038687

Fasham, M. J. R. (1977). A Comparison of Nonmetric Multidimensional Scaling, Principal Components and Reciprocal Averaging for the Ordination of Simulated Coenoclines, and Coenoplanes. *Ecology*, *58*(3), 551–561. https://doi.org/10.2307/1939004

Feakins, S. J., Levin, N. E., Liddy, H. M., Sieracki, A., Eglinton, T. I., & Bonnefille, R. (2013). Northeast african vegetation change over 12 m.y. *Geology*, *41*(3), 295–298. https://doi.org/10.1130/G33845.1

Feakins, S. J., Wu, M. S., Ponton, C., & Tierney, J. E. (2019). Biomarkers reveal abrupt switches in hydroclimate during the last glacial in southern California. *Earth and Planetary Science Letters*, *515*, 164–172. https://doi.org/10.1016/j.epsl.2019.03.024

Forester, R. M., Lowenstein, T. K., & Spencer, R. J. (2005). An ostracode based paleolimnologic and paleohydrologic history of Death Valley: 200 to 0 ka. *GSA Bulletin*, *117*(11–12), 1379–1386. https://doi.org/10.1130/B25637.1

Freimuth, E. J., Diefendorf, A. F., Lowell, T. V., & Wiles, G. C. (2019). Sedimentary n-alkanes and n-alkanoic acids in a temperate bog are biased toward woody plants. *Organic Geochemistry*, *128*, 94–107. https://doi.org/10.1016/j.orggeochem.2019.01.006

Friedman, I., Smith, G. I., Gleason, J. D., Warden, A., & Harris, J. M. (1992). Stable isotope composition of waters in southeastern California 1. Modern precipitation. *Journal of Geophysical Research*, *97*(D5), 5795. https://doi.org/10.1029/92JD00184

Friedman, I., Harris, J. M., Smith, G. I., & Johnson, C. A. (2002). Stable isotope composition of waters in the Great Basin, United States 1. Air-mass trajectories. *Journal of Geophysical Research: Atmospheres*, *107*(D19), ACL 14-1. https://doi.org/10.1029/2001JD000565

Glover, K. C., MacDonald, G. M., Kirby, M. E., Rhodes, E. J., Stevens, L., Silveira, E., et al. (2017). Evidence for orbital and North Atlantic climate forcing in alpine Southern California between 125 and 10 ka from multi-proxy analyses of Baldwin Lake. *Quaternary Science Reviews*, *167*, 47–62. https://doi.org/10.1016/J.QUASCIREV.2017.04.028

He, Y., Wang, H., Meng, B., Liu, H., Zhou, A., Song, M., et al. (2020). Appraisal of alkenone- and archaeal ether-based salinity indicators in mid-latitude Asian lakes. *Earth and Planetary Science Letters*, *538*, 116236.

Hendy, C. H. (1971). The isotopic geochemistry of speleothems—I. The calculation of the effects of different modes of formation on the isotopic composition of speleothems and their applicability as palaeoclimatic indicators. *Geochimica et Cosmochimica Acta*, *35*(8), 801–824. https://doi.org/10.1016/0016-7037(71)90127-X

Herbert, T. D., Yasuda, M., & Burnett, C. (1995). Glacial-Interglacial Sea-Surface Temperature Record Inferred from Alkenone Unsaturation indices, Site 893, Santa Barbara Basin. In *Proceedings of the Ocean Drilling Program, 146 Part 2 Scientific Results* (Vol. 146). https://doi.org/10.2973/odp.proc.sr.146-2.301.1995

Herbert, T. D., Schuffert, J. D., Andreasen, D., Heusser, L., Lyle, M., Mix, A., et al. (2001). Collapse of the California current during glacial maxima linked to climate change on land. *Science*, *293*(5527), 71–76. https://doi.org/10.1126/SCIENCE.1059209

Heusser, L. E., Kirby, M. E., & Nichols, J. E. (2015). Pollen-based evidence of extreme drought during the last Glacial (32.6-9.0 ka) in coastal southern California. *Quaternary Science Reviews*, *126*, 242–253. https://doi.org/10.1016/j.quascirev.2015.08.029

Holmgren, C. A., Betancourt, J. L., & Rylander, K. A. (2010). A long-term vegetation history of the Mojave-Colorado desert ecotone at Joshua Tree National Park. *Journal of*

Quaternary Science, *25*(2), 222–236. https://doi.org/10.1002/jqs.1313

Hopmans, E. C., Schouten, S., & Sinninghe Damsté, J. S. (2016). The effect of improved chromatography on GDGT-based palaeoproxies. *Organic Geochemistry*, *93*, 1–6. https://doi.org/10.1016/j.orggeochem.2015.12.006

Huth, T. E., Passey, B. H., Cole, J. E., Lachniet, M. S., McGee, D., Denniston, R. F., et al. (2022). A framework for triple oxygen isotopes in speleothem paleoclimatology. *Geochimica et Cosmochimica Acta*, *319*, 191–219. https://doi.org/10.1016/J.GCA.2021.11.002

Jacobel, A. W., McManus, J. F., Anderson, R. F., & Winckler, G. (2017). Climate-related response of dust flux to the central equatorial Pacific over the past 150 kyr. *Earth and Planetary Science Letters*, *457*, 160–172. https://doi.org/10.1016/J.EPSL.2016.09.042

Jacobel, Allison W, McManus, J. F., Anderson, R. F., & Winckler, G. (2016). Large deglacial shifts of the Pacific intertropical convergence zone. *Nature Communications*, *7*(1), 1–7.

Jannik, N. O., Phillips, F. M., Smith, G. I., & Elmore, D. (1991). A 36Cl chronology of lacustrine sedimentation in the Pleistocene Owens River system. *Geological Society of America Bulletin*, *103*(9), 1146–1159.

Jasechko, S., Lechler, A., Pausata, F. S. R., Fawcett, P. J., Gleeson, T., Cendon, D. I., et al. (2015). Late-glacial to late-Holocene shifts in global precipitation δ18O. *Climate of the Past*, *11*(10), 1375–1393. https://doi.org/10.5194/cp-11-1375-2015

Jayko, A. S., Forester, R. M., Kaufman, D. S., Phillips, F. M., Yount, J. C., McGeehin, J., & Mahan, S. A. (2008). Late Pleistocene lakes and wetlands, Panamint Valley, Inyo County, California. In *Special Paper of the Geological Society of America* (Vol. 439, pp. 151–184). https://doi.org/10.1130/2008.2439(07)

De Jonge, C., Kuramae, E. E., Radujković, D., Weedon, J. T., Janssens, I. A., & Peterse, F. (2021). The influence of soil chemistry on branched tetraether lipids in mid- and high latitude soils: Implications for brGDGT- based paleothermometry. *Geochimica et Cosmochimica Acta*, *310*, 95–112. https://doi.org/10.1016/j.gca.2021.06.037

De Jonge, Cindy, Hopmans, E. C., Zell, C. I., Kim, J. H., Schouten, S., & Sinninghe Damsté, J. S. (2014). Occurrence and abundance of 6-methyl branched glycerol dialkyl glycerol tetraethers in soils: Implications for palaeoclimate reconstruction. *Geochimica et Cosmochimica Acta*, *141*, 97–112. https://doi.org/10.1016/j.gca.2014.06.013

Jouzel, J., Barkov, N. I., Barnola, J. M., Bender, M., Chappellaz, J., Genthon, C., et al. (1993). Extending the Vostok ice-core record of palaeoclimate to the penultimate glacial period. *Nature 1993 364:6436*, *364*(6436), 407–412. https://doi.org/10.1038/364407a0

Kim, S. T., & O'Neil, J. R. (1997). Equilibrium and nonequilibrium oxygen isotope effects in synthetic carbonates. *Geochimica et Cosmochimica Acta*, *61*(16), 3461–3475. https://doi.org/10.1016/S0016-7037(97)00169-5

Koehler, P. A., Anderson, R. S., & Spaulding, W. G. (2005). Development of vegetation in the Central Mojave Desert of California during the late Quaternary. *Palaeogeography, Palaeoclimatology, Palaeoecology*, *215*(3–4), 297–311. Retrieved from https://www.researchgate.net/publication/222663179_Development_of_vegetation_in_the_Central_Mojave_Desert_of_California_during_the_late_Quaternary

Kulongoski, J. T., Hilton, D. R., Izbicki, J. A., & Belitz, K. (2009). Evidence for prolonged El Nino-like conditions in the Pacific during the Late Pleistocene: a 43 ka noble gas record from California groundwaters. *Quaternary Science Reviews*, *28*(23–24), 2465–2473. https://doi.org/10.1016/J.QUASCIREV.2009.05.008

Lachniet, M., Asmerom, Y., Polyak, V., & Denniston, R. (2017). Arctic cryosphere and Milankovitch forcing of Great Basin paleoclimate. *Scientific Reports 2017 7:1*, *7*(1), 1–10. https://doi.org/10.1038/s41598-017-13279-2

Lachniet, M. S. (2016). A Speleothem Record of Great Basin Paleoclimate: The Leviathan Chronology, Nevada. In *Developments in Earth Surface Processes* (Vol. 20, pp. 551–569). Elsevier B.V. https://doi.org/10.1016/B978-0-444-63590-7.00020-2

Lachniet, Matthew S., Denniston, R. F., Asmerom, Y., & Polyak, V. J. (2014). Orbital control of western North America atmospheric circulation and climate over two glacial cycles. *Nature Communications*, *5*(1), 3805. https://doi.org/10.1038/ncomms4805

Lin, J. C., Broecker, W. S., Hemming, S. R., Hajdas, I., Anderson, R. F., Smith, G. I., et al. (1998). A Reassessment of U-Th and 14C Ages for Late-Glacial High-Frequency Hydrological Events at Searles Lake, California. *Quaternary Research*, *49*, 11–23. https://doi.org/10.1006/qres.1997.1949

Lisiecki, L. E., & Raymo, M. E. (2005). A Pliocene-Pleistocene stack of 57 globally distributed benthic δ 18O records. *Paleoceanography*, *20*(1), 1–17. https://doi.org/10.1029/2004PA001071

Litwin, R. J., Smoot, J. P., Durika, N. J., & Smith, G. I. (1999). Calibrating Late Quaternary terrestrial climate signals: Radiometrically dated pollen evidence from the southern Sierra Nevada, USA. *Quaternary Science Reviews*. https://doi.org/10.1016/S0277-3791(98)00111-5

Loomis, S. E., Russell, J. M., Heureux, A. M., D'Andrea, W. J., & Sinninghe Damsté, J. S. (2014). Seasonal variability of branched glycerol dialkyl glycerol tetraethers (brGDGTs) in a temperate lake system. *Geochimica et Cosmochimica Acta*, *144*, 173–187. https://doi.org/10.1016/j.gca.2014.08.027

Lüthi, D., Le Floch, M., Bereiter, B., Blunier, T., Barnola, J.-M., Siegenthaler, U., et al. (2008). High-resolution carbon dioxide concentration record 650,000–800,000 years before present. *Nature*, *453*(7193), 379–382. https://doi.org/10.1038/nature06949

Lyle, M., Heusser, L., Ravelo, C., Andreasen, D., Olivarez Lyle, A., & Diffenbaugh, N. (2010). Pleistocene water cycle and eastern boundary current processes along the California continental margin. *Paleoceanography*, *25*(4). https://doi.org/10.1029/2009PA001836

Martínez-Sosa, P., Tierney, J. E., Stefanescu, I. C., Dearing Crampton-Flood, E., Shuman, B. N., & Routson, C. (2021). A global Bayesian temperature calibration for lacustrine brGDGTs. *Geochimica et Cosmochimica Acta*, *305*, 87–105. https://doi.org/10.1016/J.GCA.2021.04.038

McGee, D., Moreno-Chamarro, E., Marshall, J., & Galbraith, E. D. (2018). Western U.S. lake expansions during Heinrich stadials linked to Pacific Hadley circulation. *Science Advances*, *4*(11), eaav0118. https://doi.org/10.1126/sciadv.aav0118

McGee, David. (2020, January 3). Glacial-Interglacial Precipitation Changes. *Annual Review of Marine Science*. Annual Reviews. https://doi.org/10.1146/annurev-marine-010419-010859

Moseley, G. E., Edwards, R. L., Wendt, K. A., Cheng, H., Dublyansky, Y., Lu, Y., et al. (2016). Reconciliation of the Devils Hole climate record with orbital forcing. *Science (New York, N.Y.)*, *351*(6269), 165–8. https://doi.org/10.1126/science.aad4132

Olson, K. J., & Lowenstein, T. K. (2021). Searles Lake evaporite sequences: Indicators of late Pleistocene/Holocene lake temperatures, brine evolution, and pCO2. *GSA Bulletin*.

https://doi.org/10.1130/B35857.1

Oster, J. L., Ibarra, D. E., Winnick, M. J., & Maher, K. (2015). Steering of westerly storms over western North America at the Last Glacial Maximum. *Nature Geoscience*, *8*(3), 201–205. https://doi.org/10.1038/ngeo2365

Pancost, R. D., Hopmans, E. C., & Sinninghe Damsté, J. S. (2001). Archaeal lipids in Mediterranean cold seeps: molecular proxies for anaerobic methane oxidation. *Geochimica et Cosmochimica Acta*, *65*(10), 1611–1627. https://doi.org/10.1016/S0016-7037(00)00562-7

Patten, D. T., Rouse, L., & Stromberg, J. C. (2008). Isolated spring wetlands in the Great Basin and Mojave deserts, USA: Potential response of vegetation to groundwater withdrawal. *Environmental Management*, *41*(3), 398–413. https://doi.org/10.1007/S00267-007-9035-9

Peaple, M. D., Tierney, J. E., McGee, D., Lowenstein, T. K., Bhattacharya, T., & Feakins, S. J. (2021). Identifying plant wax inputs in lake sediments using machine learning. *Organic Geochemistry*, *156*, 104222. https://doi.org/10.1016/J.ORGGEOCHEM.2021.104222

Pierce, D. W., Cayan, D. R., Das, T., Maurer, E. P., Miller, N. L., Bao, Y., et al. (2013). The Key Role of Heavy Precipitation Events in Climate Model Disagreements of Future Annual Precipitation Changes in California. *Journal of Climate*, *26*(16), 5879–5896. https://doi.org/10.1175/JCLI-D-12-00766.1

Reheis, M. C., Stine, S., & Sarna-Wojcicki, A. M. (2002). Drainage reversals in Mono Basin during the late Pliocene and Pleistocene. *Geological Society of America Bulletin*, *114*(8), 991–1006.

Rimmer, A., Gal, G., Opher, T., Lechinsky, Y., & Yacobi, Y. Z. (2011). Mechanisms of long-term variations in the thermal structure of a warm lake. *Limnology and Oceanography*, *56*(3), 974–988. https://doi.org/10.4319/LO.2011.56.3.0974

Roberts, S. M., & Spencer, R. J. (1998). A desert responds to Pleistocene climate change: Saline lacustrine sediments, Death Valley, California, USA. In *Quaternary Deserts and Climatic Change* (pp. 357–370). CRC Press. https://doi.org/10.1201/9781003077862-37

Russell, J. M., Hopmans, E. C., Loomis, S. E., Liang, J., & Sinninghe Damsté, J. S. (2018). Distributions of 5- and 6-methyl branched glycerol dialkyl glycerol tetraethers (brGDGTs) in East African lake sediment: Effects of temperature, pH, and new lacustrine paleotemperature calibrations. *Organic Geochemistry*, *117*, 56–69. https://doi.org/10.1016/J.ORGGEOCHEM.2017.12.003

Schouten, S., Wakeham, S. G., & Damsté, J. S. S. (2001). Evidence for anaerobic methane oxidation by archaea in euxinic waters of the Black Sea. *Organic Geochemistry*, *32*(10), 1277–1281. https://doi.org/10.1016/S0146-6380(01)00110-3

Schouten, S., Hopmans, E. C., Schefuß, E., & Sinninghe Damsté, J. S. (2002). Distributional veriations in marine crenarchaeol membrane lipids: a new tool for reconstructing ancient sea water temperatures? *Earth and Planetary Science Letters*, *204*, 265–274. https://doi.org/10.1016/S0012-821X(03)00193-6

Schouten, S., Rijpstra, W. I. C., Durisch-Kaiser, E., Schubert, C. J., & Sinninghe Damsté, J. S. (2012). Distribution of glycerol dialkyl glycerol tetraether lipids in the water column of Lake Tanganyika. *Organic Geochemistry*, *53*, 34–37. https://doi.org/10.1016/J.ORGGEOCHEM.2012.01.009

Schouten, S., Hopmans, E. C., & Sinninghe Damsté, J. S. (2013). The organic geochemistry

of glycerol dialkyl glycerol tetraether lipids: A review. *Organic Geochemistry*, *54*, 19–61. https://doi.org/10.1016/J.ORGGEOCHEM.2012.09.006

Seltzer, A. M., Ng, J., Aeschbach, W., Kipfer, R., Kulongoski, J. T., Severinghaus, J. P., & Stute, M. (2021). Widespread six degrees Celsius cooling on land during the Last Glacial Maximum. *Nature*, *593*(7858), 228–232. https://doi.org/10.1038/S41586-021-03467-6

Sinninghe Damsté, J. S., Schouten, S., Hopmans, E. C., Van Duin, A. C. T., & Geenevasen, J. A. J. (2002). Crenarchaeol. *Journal of Lipid Research*, *43*(10), 1641–1651. https://doi.org/10.1194/JLR.M200148-JLR200

Sinninghe Damsté, J. S., Ossebaar, J., Schouten, S., & Verschuren, D. (2012). Distribution of tetraether lipids in the 25-ka sedimentary record of Lake Challa: extracting reliable TEX86 and MBT/CBT palaeotemperatures from an equatorial African lake. *Quaternary Science Reviews*, *50*, 43–54. https://doi.org/10.1016/J.QUASCIREV.2012.07.001

Sinninghe Damsté, J. S., Rijpstra, W. I. C., Hopmans, E. C., Jung, M. Y., Kim, J. G., Rhee, S. K., et al. (2012). Intact polar and core glycerol dibiphytanyl glycerol tetraether lipids of group I.1a and I.1b Thaumarchaeota in soil. *Applied and Environmental Microbiology*, *78*(19), 6866–6874. https://doi.org/10.1128/AEM.01681-12

Smith, G. I. (2009). Late Cenozoic geology and lacustrine history of Searles Valley, inyo and San Bernardino counties, California. *US Geological Survey Professional Paper*. https://doi.org/10.3133/pp1727

Smith, G. I., Barczak, V. J., Moulton, G. F., & Liddicoat, J. C. (1983). *Core KM-3, a surface-to-bedrock record of late Cenozoic sedimentation in Searles Valley, California*. *Professional Paper*. https://doi.org/10.3133/PP1256

Stefanescu, I. C., Shuman, B. N., & Tierney, J. E. (2021). Temperature and water depth effects on brGDGT distributions in sub-alpine lakes of mid-latitude North America. *Organic Geochemistry*, *152*, 104174. https://doi.org/10.1016/J.ORGGEOCHEM.2020.104174

Tabor, C., Lofverstrom, M., Oster, J., Wortham, B., de Wet, C., Montañez, I., et al. (2021). A mechanistic understanding of oxygen isotopic changes in the Western United States at the Last Glacial Maximum. *Quaternary Science Reviews*, *274*, 107255. https://doi.org/10.1016/J.QUASCIREV.2021.107255

Thompson, R. S., & Anderson, K. H. (2000). Biomes of western North America at 18,000, 6000 and 0 14C yr BP reconstructed from pollen and packrat midden data. *Journal of Biogeography*, *27*(3), 555–584. https://doi.org/10.1046/J.1365-2699.2000.00427.X

Tierney, J. E., Russell, J. M., & Huang, Y. (2010). A molecular perspective on Late Quaternary climate and vegetation change in the Lake Tanganyika basin, East Africa. *Quaternary Science Reviews*, *29*(5–6), 787–800. https://doi.org/10.1016/J.QUASCIREV.2009.11.030

Tierney, J. E., Mayes, M. T., Meyer, N., Johnson, C., Swarzenski, P. W., Cohen, A. S., & Russell, J. M. (2010). Late-twentieth-century warming in Lake Tanganyika unprecedented since AD 500. *Nature Geoscience 2010 3:6*, *3*(6), 422–425. https://doi.org/10.1038/ngeo865

Verschuren, D., Sinninghe Damsté, J. S., Moernaut, J., Kristen, I., Blaauw, M., Fagot, M., & Haug, G. H. (2009). Half-precessional dynamics of monsoon rainfall near the East African Equator. *Nature 2009 462:7273*, *462*(7273), 637–641. https://doi.org/10.1038/nature08520

Wang, H., He, Y., Liu, W., Zhou, A., Kolpakova, M., Krivonogov, S., & Liu, Z. (2019). Lake Water Depth Controlling Archaeal Tetraether Distributions in Midlatitude Asia: Implications for Paleo Lake-Level Reconstruction. *Geophysical Research Letters*, *46*(10), 5274–5283. https://doi.org/10.1029/2019GL082157

Wang, Huanye, Liu, W., Zhang, C. L., Jiang, H., Dong, H., Lu, H., & Wang, J. (2013). Assessing the ratio of archaeol to caldarchaeol as a salinity proxy in highland lakes on the northeastern Qinghai–Tibetan Plateau. *Organic Geochemistry*, *54*, 69–77. https://doi.org/10.1016/J.ORGGEOCHEM.2012.09.011

Wang, Huanye, Liu, W., He, Y., Zhou, A., Zhao, H., Liu, H., et al. (2021). Salinity-controlled isomerization of lacustrine brGDGTs impacts the associated MBT5ME' terrestrial temperature index. *Geochimica et Cosmochimica Acta*, *305*, 33–48. https://doi.org/10.1016/J.GCA.2021.05.004

Wang, Z., Zhang, F., Cao, Y., Hu, J., Wang, H., Lu, H., et al. (2022). Linking sedimentary and speleothem precipitation isotope proxy records to improve lacustrine and marine 14C chronologies. *Quaternary Science Reviews*, *282*, 107444. https://doi.org/10.1016/J.QUASCIREV.2022.107444

Weber, Y., Damsté, J. S. S., Zopfi, J., De Jonge, C., Gilli, A., Schubert, C. J., et al. (2018). Redox-dependent niche differentiation provides evidence for multiple bacterial sources of glycerol tetraether lipids in lakes. *Proceedings of the National Academy of Sciences of the United States of America*, *115*(43), 10926–10931. https://doi.org/10.1073/PNAS.1805186115/SUPPL_FILE/PNAS.1805186115.SD02.XLS

Wendt, K. A., Dublyansky, Y. V., Moseley, G. E., Edwards, R. L., Cheng, H., & Spötl, C. (2018). Moisture availability in the southwest United States over the last three glacial-interglacial cycles. *Science Advances*, *4*(10), eaau1375.

Western Regional Climate Center. (2022). US COOP Station Map. Retrieved October 31, 2018, from https://wrcc.dri.edu/coopmap/

Willson, C. J., Manos, P. S., & Jackson, R. B. (2008). Hydraulic traits are influenced by phylogenetic history in the drought-resistant, invasive genus Juniperus (Cupressaceae). *American Journal of Botany*, *95*(3), 299–314. https://doi.org/10.3732/AJB.95.3.299

Winograd, I. J., Coplen, T. B., Landwehr, J. M., Riggs, A. C., Ludwig, K. R., Szabo, B. J., et al. (1992). Continuous 500,000-year climate record from vein calcite in Devils Hole, Nevada. *Science*, *258*(5080), 255–260. https://doi.org/10.1126/science.258.5080.255

Wood, G. D. (2000). Pollen analysis of death valley sediments deposited between 166 and 114 ka. *Palynology*, *24*(1), 49–61. https://doi.org/10.1080/01916122.2000.9989537

Woolfenden, W. B. (2003). A 180,000-year pollen record from Owens Lake, CA: Terrestrial vegetation change on orbital sales. *Quaternary Research*, *59*(3), 430–444. https://doi.org/10.1016/S0033-5894(03)00033-4

References from the supporting information

Aichner, B., Herzschuh, U., & Wilkes, H. (2010). Influence of aquatic macrophytes on the stable carbon isotopic signatures of sedimentary organic matter in lakes on the Tibetan Plateau. *Organic Geochemistry*, *41*(7), 706–718. https://doi.org/10.1016/j.orggeochem.2010.02.002

Aichner, B., Hilt, S., Périllon, C., Gillefalk, M., & Sachse, D. (2017). Biosynthetic hydrogen isotopic fractionation factors during lipid synthesis in submerged aquatic macrophytes:

Effect of groundwater discharge and salinity. *Organic Geochemistry*, *113*, 10–16. https://doi.org/10.1016/J.ORGGEOCHEM.2017.07.021

Bi, X., Sheng, G., Liu, X., Li, C., & Fu, J. (2005). Molecular and carbon and hydrogen isotopic composition of n-alkanes in plant leaf waxes. *Organic Geochemistry*, *36*(10), 1405–1417. https://doi.org/10.1016/J.ORGGEOCHEM.2005.06.001

Czop, M., Motyka, J., Sracek, O., & Szuwarzyński, M. (2011). Geochemistry of the hyperalkaline Gorka pit lake (pH>13) in the Chrzanow region, southern Poland. *Water, Air, and Soil Pollution*, *214*(1–4), 423–434. https://doi.org/10.1007/s11270-010-0433-x

Dearing Crampton-Flood, E., Tierney, J. E., Peterse, F., Kirkels, F. M. S. A., & Sinninghe Damsté, J. S. (2020). BayMBT: A Bayesian calibration model for branched glycerol dialkyl glycerol tetraethers in soils and peats. *Geochimica et Cosmochimica Acta*, *268*, 142–159. https://doi.org/10.1016/j.gca.2019.09.043

Diefendorf, A. F., Leslie, A. B., & Wing, S. L. (2015). Leaf wax composition and carbon isotopes vary among major conifer groups. *Geochimica et Cosmochimica Acta*, *170*, 145–156. https://doi.org/10.1016/j.gca.2015.08.018

Feakins, S. J. (2013). Pollen-corrected leaf wax D/H reconstructions of northeast African hydrological changes during the late Miocene. *Palaeogeography, Palaeoclimatology, Palaeoecology*, *374*, 62–71. https://doi.org/10.1016/J.PALAEO.2013.01.004

Feakins, S. J., & Sessions, A. L. (2010). Controls on the D/H ratios of plant leaf waxes in an arid ecosystem. *Geochimica et Cosmochimica Acta*, *74*(7), 2128–2141. https://doi.org/10.1016/J.GCA.2010.01.016

Fornace, K. L., Whitney, B. S., Galy, V., Hughen, K. A., & Mayle, F. E. (2016). Late Quaternary environmental change in the interior South American tropics: new insight from leaf wax stable isotopes. *Earth and Planetary Science Letters*, *438*, 75–85. https://doi.org/10.1016/J.EPSL.2016.01.007

Freimuth, E. J., Diefendorf, A. F., & Lowell, T. V. (2017). Hydrogen isotopes of n-alkanes and n-alkanoic acids as tracers of precipitation in a temperate forest and implications for paleorecords. *Geochimica et Cosmochimica Acta*, *206*, 166–183. https://doi.org/10.1016/J.GCA.2017.02.027

Hay, R. L., Guldman, S. G., Matthews, J. C., Lander, R. H., Duffin, M. E., & Kyser, T. K. (1991). Clay mineral diagenesis in core KM-3 of Searles Lake, California. *Clays and Clay Minerals*, *39*(1), 84–96. https://doi.org/10.1346/CCMN.1991.0390111

Inglis, G. N., Carmichael, M. J., Farnsworth, A., Lunt, D. J., & Pancost, R. D. (2020). A long-term, high-latitude record of Eocene hydrological change in the Greenland region. *Palaeogeography, Palaeoclimatology, Palaeoecology*, *537*, 109378. https://doi.org/10.1016/J.PALAEO.2019.109378

Krull, E., Sachse, D., Mügler, I., Thiele, A., & Gleixner, G. (2006). Compound-specific δ13C and δ2H analyses of plant and soil organic matter: A preliminary assessment of the effects of vegetation change on ecosystem hydrology. *Soil Biology and Biochemistry*, *38*(11), 3211–3221. https://doi.org/10.1016/J.SOILBIO.2006.04.008

Lisiecki, L. E., & Raymo, M. E. (2005). A Pliocene-Pleistocene stack of 57 globally distributed benthic δ18 O records. *Paleoceanography*, *20*(1), n/a-n/a. https://doi.org/10.1029/2004PA001071

Litwin, R. J., Smoot, J. P., Durika, N. J., & Smith, G. I. (1999). Calibrating Late Quaternary terrestrial climate signals: Radiometrically dated pollen evidence from the southern Sierra Nevada, USA. *Quaternary Science Reviews*. https://doi.org/10.1016/S0277-3791(98)00111-5

Liu, W., Yang, H., & Li, L. (2006). Hydrogen isotopic compositions of n-alkanes from

terrestrial plants correlate with their ecological life forms. *GLOB AL CHANGE AND CONSERVATION ECOLOGY*, *150*, 330–338. https://doi.org/10.1007/s00442-006-0494-0

Makou, M., Eglinton, T., McIntyre, C., Montluçon, D., Antheaume, I., & Grossi, V. (2018). Plant Wax n -Alkane and n -Alkanoic Acid Signatures Overprinted by Microbial Contributions and Old Carbon in Meromictic Lake Sediments. *Geophysical Research Letters*, *45*(2), 1049–1057. https://doi.org/10.1002/2017GL076211

Martínez-Sosa, P., Tierney, J. E., Stefanescu, I. C., Dearing Crampton-Flood, E., Shuman, B. N., & Routson, C. (2021). A global Bayesian temperature calibration for lacustrine brGDGTs. *Geochimica et Cosmochimica Acta*, *305*, 87–105. https://doi.org/10.1016/J.GCA.2021.04.038

McCallister, S. L., & Del Giorgio, P. A. (2008). Direct measurement of the δ13C signature of carbon respired by bacteria in lakes: Linkages to potential carbon sources, ecosystem baseline metabolism, and CO2 fluxes. *Limnology and Oceanography*, *53*(4), 1204–1216. https://doi.org/10.4319/lo.2008.53.4.1204

Nobel, P. S., & Bobich, E. G. (2002). Initial Net CO2 Uptake Responses and Root Growth for a CAM Community Placed in a Closed Environment. *Annals of Botany*, *90*(5), 593–598. https://doi.org/10.1093/AOB/MCF229

Peaple, M. D., Tierney, J. E., McGee, D., Lowenstein, T. K., Bhattacharya, T., & Feakins, S. J. (2021). Identifying plant wax inputs in lake sediments using machine learning. *Organic Geochemistry*, *156*, 104222. https://doi.org/10.1016/J.ORGGEOCHEM.2021.104222

Pennington, W. (1979). The origin of pollen in lakes sedimetns: an enclosed lake compared with one recieiving inflow stream. *New Phytologist*, *83*(1), 189–213. https://doi.org/10.1111/j.1469-8137.1979.tb00741.x

Russell, J. M., Hopmans, E. C., Loomis, S. E., Liang, J., & Sinninghe Damsté, J. S. (2018). Distributions of 5- and 6-methyl branched glycerol dialkyl glycerol tetraethers (brGDGTs) in East African lake sediment: Effects of temperature, pH, and new lacustrine paleotemperature calibrations. *Organic Geochemistry*, *117*, 56–69. https://doi.org/10.1016/J.ORGGEOCHEM.2017.12.003

Sachse, D., Billault, I., Bowen, G. J., Chikaraishi, Y., Dawson, T. E., Feakins, S. J., et al. (2012). Molecular Paleohydrology: Interpreting the Hydrogen-Isotopic Composition of Lipid Biomarkers from Photosynthesizing Organisms, *40*(1). https://doi.org/10.1146/annurev-earth-042711-105535

Tamalavage, A. E., van Hengstum, P. J., Louchouarn, P., Fall, P. L., Donnelly, J. P., Albury, N. A., et al. (2020). Plant wax evidence for precipitation and vegetation change from a coastal sinkhole lake in the Bahamas spanning the last 3000 years. *Organic Geochemistry*, *150*, 104120. https://doi.org/10.1016/J.ORGGEOCHEM.2020.104120

Tipple, B. J., & Pagani, M. (2010). A 35 Myr North American leaf-wax compound-specific carbon and hydrogen isotope record: Implications for C4 grasslands and hydrologic cycle dynamics. *Earth and Planetary Science Letters*, *299*(1–2), 250–262. https://doi.org/10.1016/J.EPSL.2010.09.006

Tipple, B. J., & Pagani, M. (2013). Environmental control on eastern broadleaf forest speciesâ€™ leaf wax distributions and D/H ratios. *Geochimica et Cosmochimica Acta*, *111*, 64–77. https://doi.org/10.1016/j.gca.2012.10.042

Turich, C., & Freeman, K. H. (2011). Archaeal lipids record paleosalinity in hypersaline systems. *Organic Geochemistry*, *42*(9), 1147–1157. https://doi.org/10.1016/J.ORGGEOCHEM.2011.06.002

Williams, D. G., & Ehleringer, J. R. (2000). Intra- and Interspecific Variation for Summer Precipitation Use in Pinyon-Juniper Woodlands. *Ecological Monographs*, *70*(4), 517. https://doi.org/10.2307/2657185

Windler, G., Tierney, J. E., Zhu, J., & Poulsen, C. J. (2020). Unraveling Glacial Hydroclimate in the Indo-Pacific Warm Pool: Perspectives From Water Isotopes. *Paleoceanography and Paleoclimatology*, *35*(12), e2020PA003985. https://doi.org/10.1029/2020PA003985

Woolfenden, W. B. (2003). A 180,000-year pollen record from Owens Lake, CA: Terrestrial vegetation change on orbital sales. *Quaternary Research*, *59*(3), 430–444. https://doi.org/10.1016/S0033-5894(03)00033-4

Xia, L., Cao, J., Stüeken, E. E., Zhi, D., Wang, T., & Li, W. (2020). Unsynchronized evolution of salinity and pH of a Permian alkaline lake influenced by hydrothermal fluids: A multi-proxy geochemical study. *Chemical Geology*, *541*, 119581. https://doi.org/10.1016/J.CHEMGEO.2020.119581

Yu, K., D'odorico, P., Collins, S. L., Carr, D., Porporato, A., Anderegg, W. R. L., et al. (2019). The competitive advantage of a constitutive CAM species over a C4 grass species under drought and CO2 enrichment. *Ecosphere*, *10*(5), e02721. https://doi.org/10.1002/ECS2.2721

Table and Figure Captions:

Table 1: Summary of proxies used in this study

Measure	Producer	Proxy information
Plant microfossils		
Pollen	Plant	Plant species
Plant wax *n*-alkanes and *n*-alkanoic acids		
abundance*	Plant	plant type, preservation
$\delta^{13}C$	Plant	C_3 vs. C_4, C_3 water stress
δD	Plant	δD precipitation
GDGTs		
BIT	Microbial	Bacteria:Archaea
BrGDGTs	Bacteria	soil or lake productivity
IsoGDGTs	Archaea	lake productivity
%GDGT-0	Archaea	lake stratification
ACE	Archaea	lake salinity
IR_{6+7ME}	Bacteria	soil or lake salinity
CBT'	Bacteria	soil or lake pH
MBT'_{5ME}	Bacteria	air temperature
TEX_{86}	Archaea	lake temperature

*& chain length distribution metrics: ACL, CPI, ML

Figure 1. Maps showing location of A) Searles Lake (red star) and climate archives referred to in the text including Owens Lake (blue circle), ODP 1012/1010 (pink circles), Devils Hole

(orange circle), Leviathan Cave, Lehman Cave, and Pinnacle Cave (black circles) B) The Lakes connected to Searles Lake during pluvial periods where M = Mono Lake, O = Owens Lake, C = China Lake, S = Searles Lake, P = Lake Panamint, M = Lake Manly. C) Map of Searles Lake during pluvial conditions highlighting inflow and outflow.

Figure 2. Vegetation reconstructions using pollen and plant wax proxies from SLAPP-SRLS17. A) Proportion of pollen taxa. B) Modelled vegetation types based on SVM machine learning of plant wax distributions in modern taxa applied to the downcore record (Peaple et al., 2021). C) Comparison between modelled desert plant types and pollen "desert shrubs" (the sum of Amaranth and Asteraceae pollen) presented as Z scores, i.e., normalized by the mean in standard deviation units. D) $\delta^{13}C_{28acid}$ and $\delta^{13}C_{31alk}$ compared to Amaranth pollen. E) δD_{28acid} and δD_{31alk}.

Figure 3. PCA to assess biomarker and pollen covariations (Shrub = sum of Amaranthaceae and Asteraceae pollen abundance).

Figure 4. Comparison of Searles Lake plant wax δD_{31alk} and calculated δD_{precip} to global climate data across two glacial-interglacial cycles showing A) Antarctic pCO_2 record (Lüthi et al., 2008), B) LR04 $\delta^{18}O$ benthic foraminifera stack (Lisiecki & Raymo, 2005), C) plant wax C_{31} *n*-alkane δD (blue curve) and inferred precipitation δD after apparent fractionation and ice volume correction (black curve). D) $BayMBT_0$ and E) shrub pollen%. Upper labels: "Hol" = Holocene, "LGM" = Last glacial maximum, "LIG" = Last interglacial, "PGM" = Penultimate glacial maximum. Lower labels: "MIS" = Marine isotope stage.

Figure 5. Comparison of plant wax and speleothem isotopic records. A) Searles Lake δD_{precip} (black, this study), Leviathan composite record $\delta^{18}O_{calcite}$ (orange; Lachniet et al., 2016) and Devils Hole $\delta^{18}O_{calcite}$ (red; Moseley et al., 2016) with the $\delta^{18}O$ axis scaled to account for the 8x greater mass dependent fractionation for hydrogen. B) Searles Lake δD_{precip} (black) and summer insolation at 65°N (gray). C) Devils Hole $\delta^{18}O_{calcite}$ and summer insolation at 65°N (gray). D) Leviathan composite record $\delta^{18}O_{calcite}$ (left) as in A but showing the individual caves, two of which (Lehman and Pinnacle), were adjusted for spatial gradients in precipitation isotopes (Lachniet et al., 2016). Black and white bars represent MIS stages. E – G) Weighted wavelet z transform frequency spectrum for the records in B, C, and D. H) 5 to 95 % quartile range for measured values (blue), and after corrections for ice volume (grey), cave temperature (Leviathan record, black bar) and plant wax $\varepsilon_{wax/w}$ (green). The $\delta^{18}O$ axis is scaled to account for the 8x difference in mass dependent fractionation between H and O. Ice volume-corrected Devils Hole shows the smallest range, whereas larger and comparable magnitudes are recorded at the temperature-corrected Leviathan composite record and Searles Lake.

Figure 6. Biomarker evidence that the late MIS 6 pluvial was a fresher water lake than the late MIS 2 pluvial. Water balance reconstructions Searles Lake: A) ACE, B) IR_{6+7me}, C) BIT D) %GDGT-0, and E) Devils Hole water table elevation (Wendt et al., 2018). Age model without tie point is plotted for all GDGT indices as a thin faint line. Terminations 1 and 2 are highlighted with yellow shading and Heinrich 1 and 11 are highlighted with blue shading. Upper labels: "LGM" = Last glacial maximum, "LIG" = Last interglacial, "PGM" = Penultimate glacial maximum. Lower labels: "MIS" = Marine isotope stage.

Figure 7. Local and regional temperature records over the past 200 kyr. A. Searles Lake (blue line; this study) and Lake Elsinore (orange line; Feakins et al., 2019) recalibrated to

MAF using Martinez Sosa et al., (2021) brGDGT temperature records, using the lake MBT'_{5Me} $BayMBT_0$ calibration to mean temperature from months above freezing (MAF) with an RMSE of 3°C. TEX_{86} calibrated to lake surface temperature (black dot) (Tierney, Mayes, et al., 2010). B) Noble gas derived ground water temperature records (Mojve: Kulongoski et al., 2009; San Diego: Seltzer et al., 2021). Comparison temperature responsive vegetation change showing C) shrub pollen % (Amaranthaceae and Asteraceae; this study). D) Alkenone based sea surface temperature (SST) records (ODP 1012, ODP 893: Herbert et al., 2001, 1995).

Figure 1.

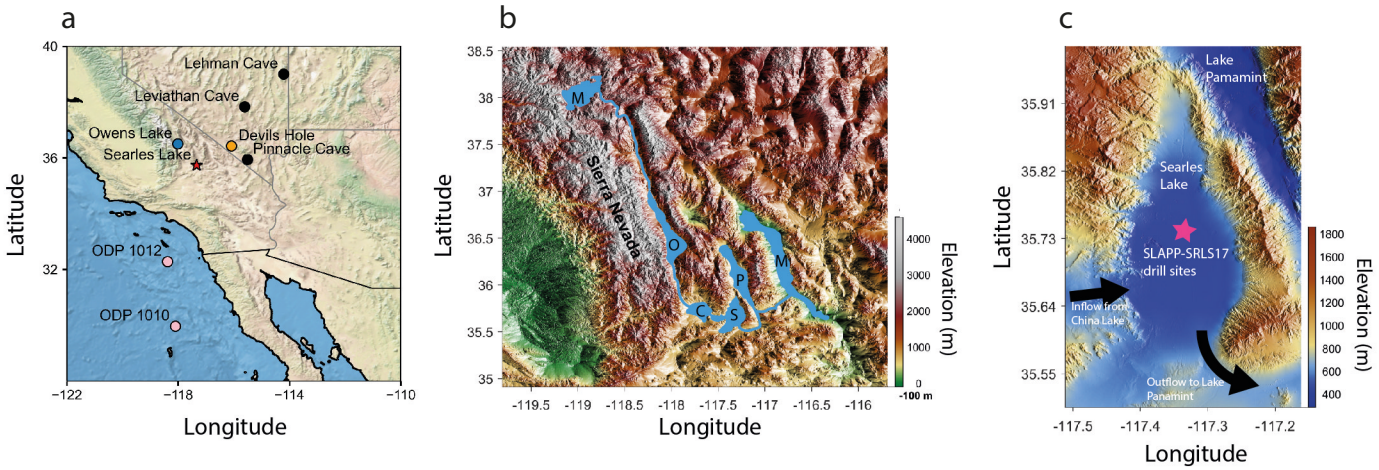
a
Lehman Cave
Leviathan Cave
Owens Lake
Searles Lake
Devils Hole
Pinnacle Cave
ODP 1012
ODP 1010
Latitude
Longitude
40
36
32
−122
−118
−114
−110
b
Sierra Nevada
M
O
P
C
S
Latitude
Longitude
Elevation (m)
38.5
38
37.5
37
36.5
36
35.5
35
-119.5
-119
-118.5
-118
-117.5
-117
-116.5
-116
4000
3000
2000
1000
0
-100 m
c
Lake Pamamint
Searles Lake
SLAPP-SRLS17 drill sites
Inflow from China Lake
Outflow to Lake Panamint
Latitude
Longitude
Elevation (m)
35.91
35.82
35.73
35.64
35.55
-117.5
-117.4
-117.3
-117.2
1800
1600
1400
1200
1000
800
600
400

Figure 2.

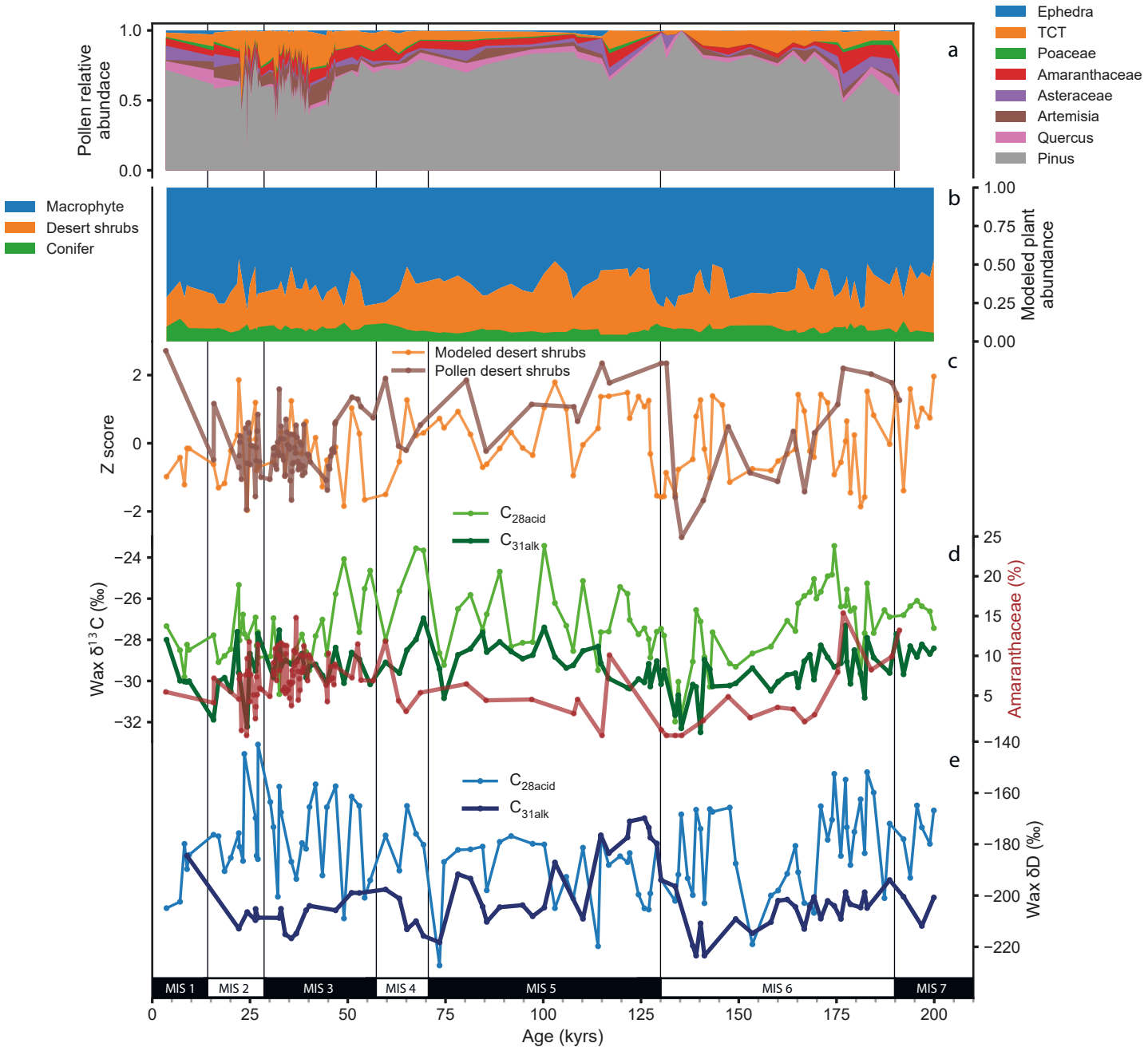
Ephedra
TCT
Poaceae
Amaranthaceae
Asteraceae
Artemisia
Quercus
Pinus
Pollen relative abundace
1.0
0.5
0.0
a
Macrophyte
Desert shrubs
Conifer
b
Modeled plant abundance
1.00
0.75
0.50
0.25
0.00
Modeled desert shrubs
Pollen desert shrubs
c
Z score
2
0
−2
C_{28acid}
C_{31alk}
d
Wax $\delta^{13}C$ (‰)
−24
−26
−28
−30
−32
Amaranthaceae (%)
25
20
15
10
5
e
−140
−160
−180
−200
−220
Wax δD (‰)
MIS 1
MIS 2
MIS 3
MIS 4
MIS 5
MIS 6
MIS 7
0
25
50
75
100
125
150
175
200
Age (kyrs)

Figure 3.

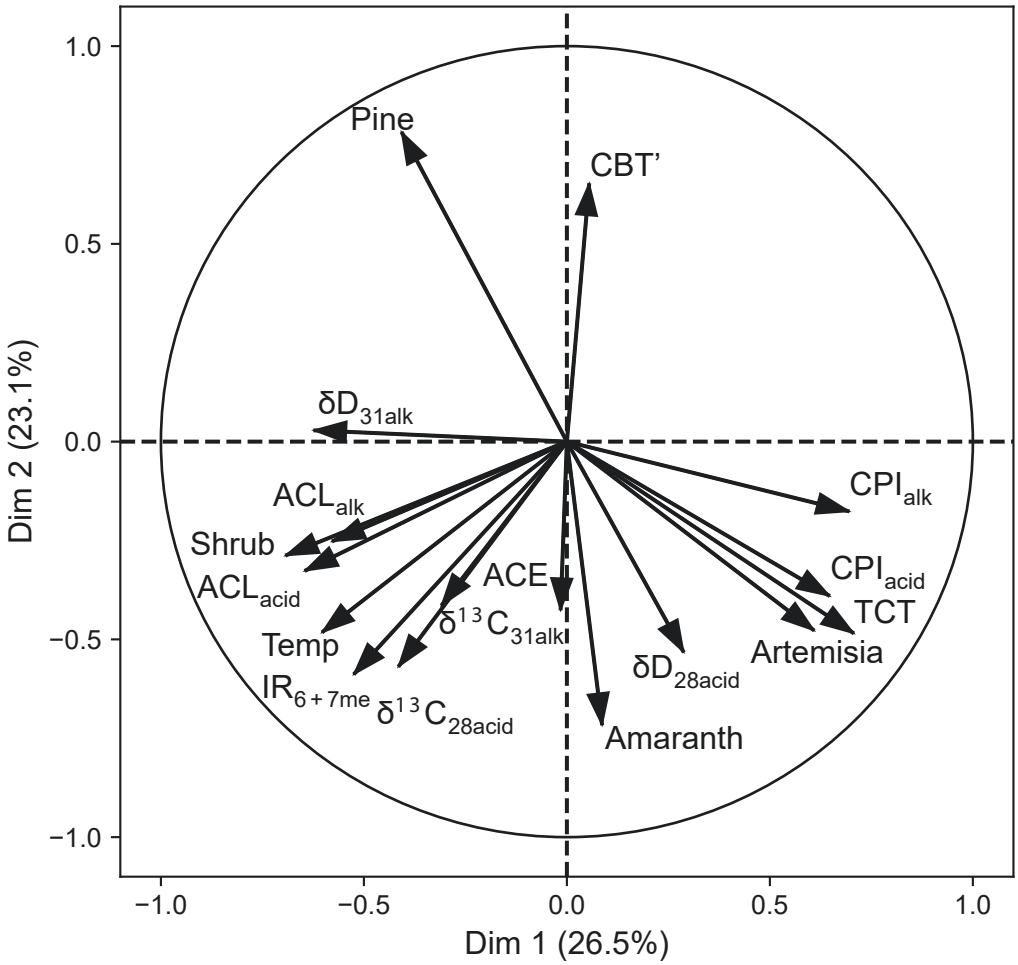
Pine
CBT'
δD31alk
ACLalk
Shrub
ACLacid
Temp
IR6+7me
δ13C28acid
ACE
δ13C31alk
δD28acid
Amaranth
CPIalk
CPIacid
TCT
Artemisia
1.0
0.5
0.0
−0.5
−1.0
−1.0
−0.5
0.0
0.5
1.0
Dim 2 (23.1%)
Dim 1 (26.5%)

Figure 4.

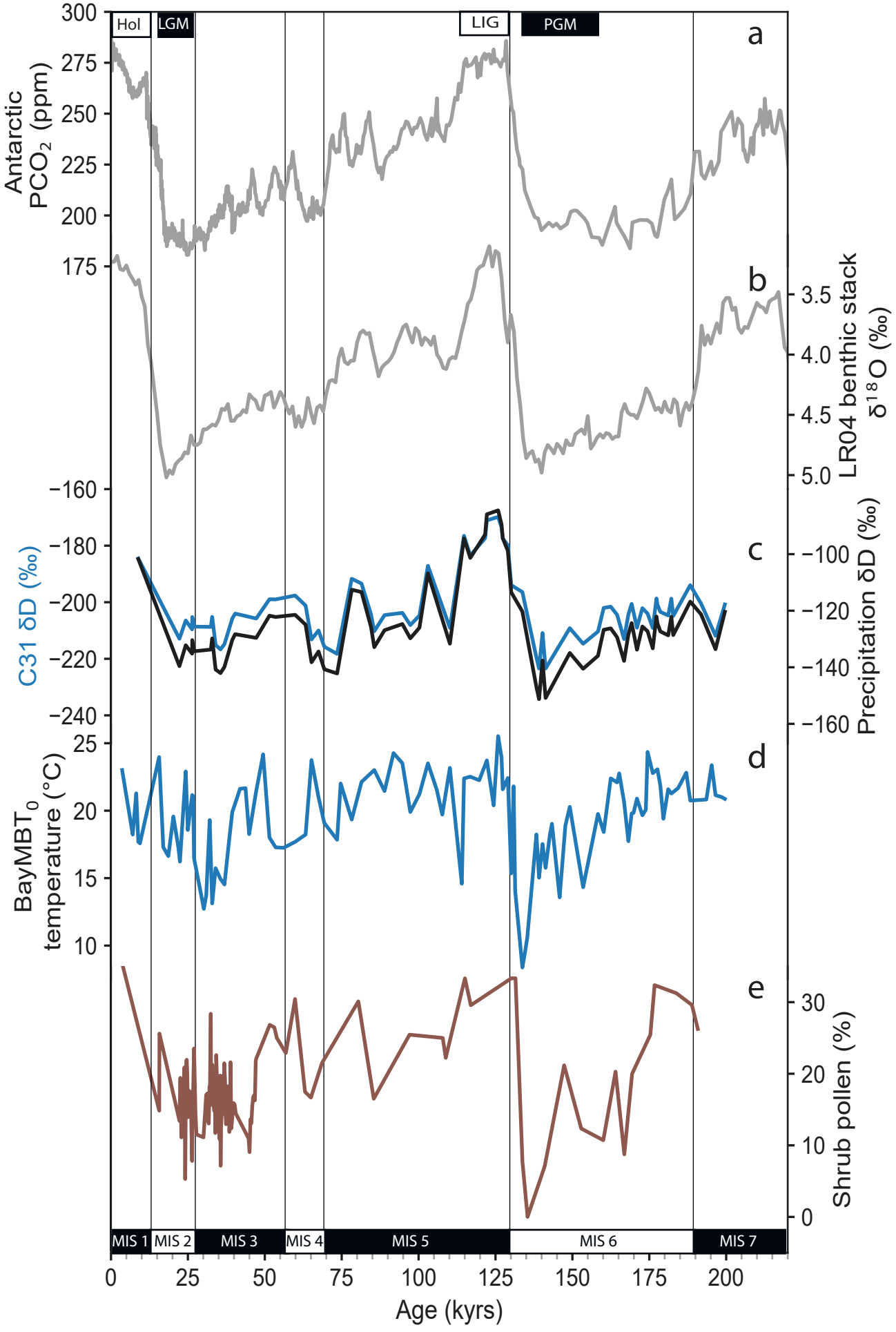
Hol
LGM
LIG
PGM
a
b
c
d
e
Antarctic PCO2 (ppm)
LR04 benthic stack δ18O (‰)
C31 δD (‰)
Precipitation δD (‰)
BayMBT0 temperature (°C)
Shrub pollen (%)
MIS 1
MIS 2
MIS 3
MIS 4
MIS 5
MIS 6
MIS 7
Age (kyrs)

Figure 5.

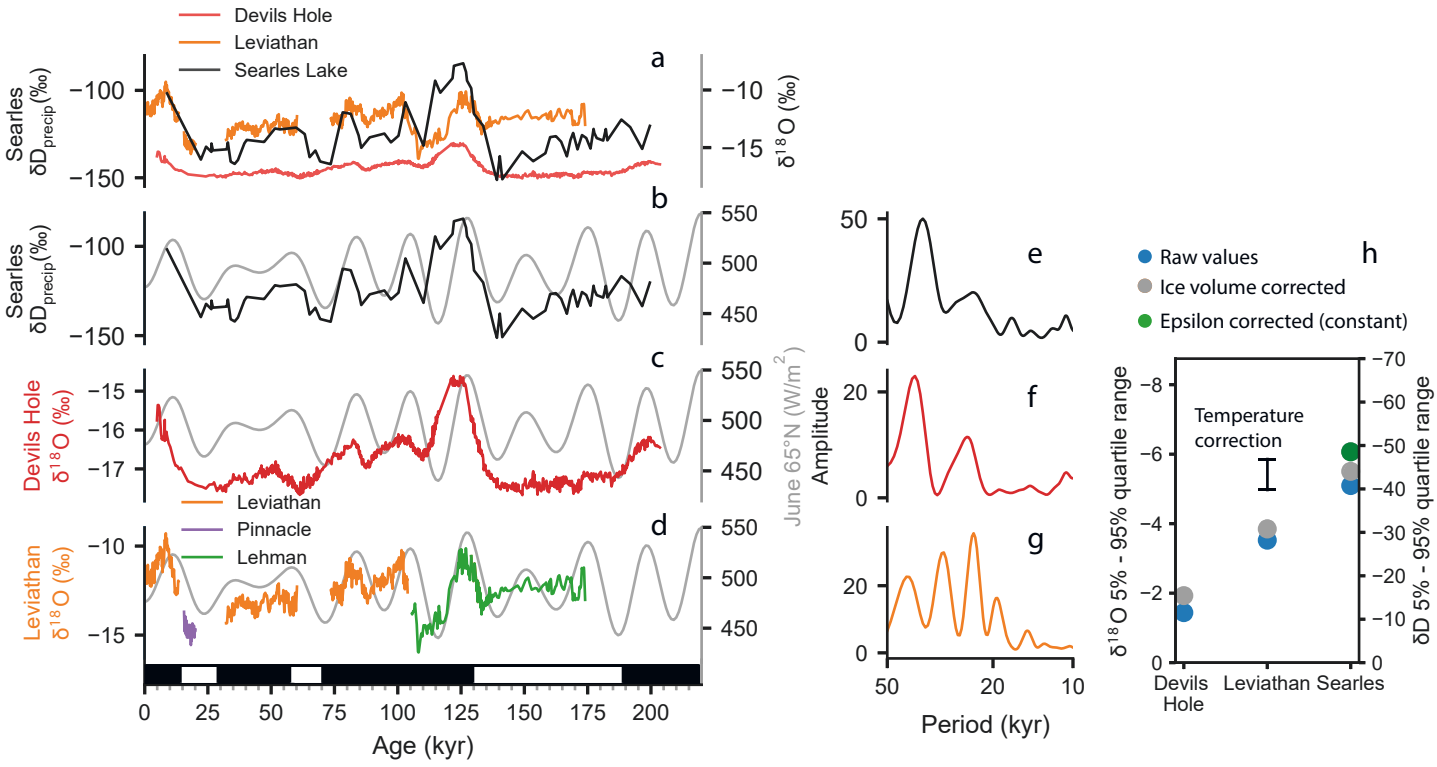
Devils Hole
Leviathan
Searles Lake
a
Searles δD_precip (‰)
−100
−150
−10
−15
δ18O (‰)
b
550
500
450
c
Devils Hole δ18O (‰)
−15
−16
−17
Leviathan
Pinnacle
Lehman
d
Leviathan δ18O (‰)
−10
−15
0
25
50
75
100
125
150
175
200
Age (kyr)
June 65°N (W/m2)
Amplitude
e
f
g
50
20
10
Period (kyr)
h
Raw values
Ice volume corrected
Epsilon corrected (constant)
Temperature correction
δ18O 5% - 95% quartile range
δD 5% - 95% quartile range
−8
−6
−4
−2
−70
−60
−50
−40
−30
−20
−10
Devils Hole
Leviathan
Searles

Figure 6.

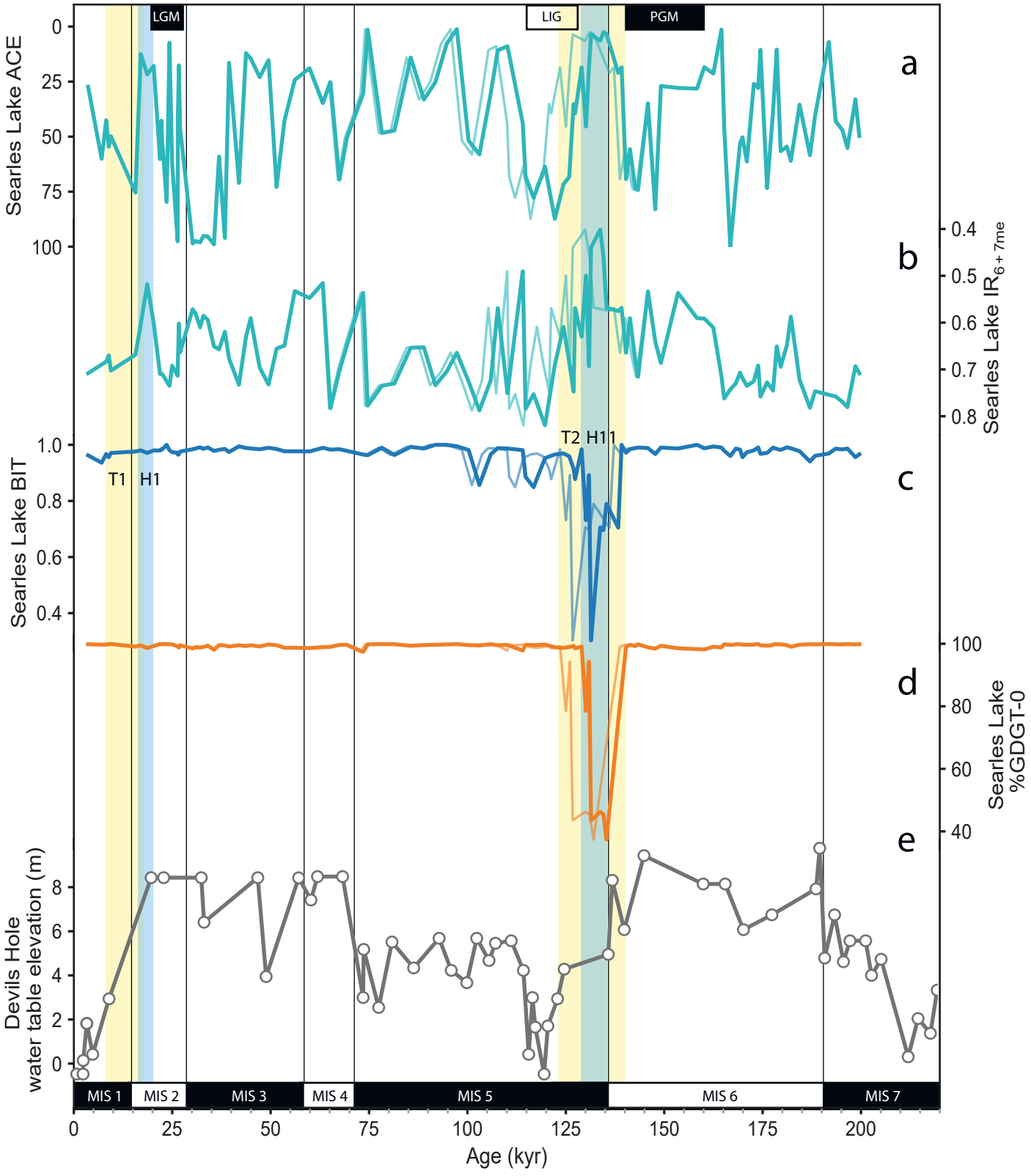
LGM
LIG
PGM
a
b
c
d
e
Searles Lake ACE
0
25
50
75
100
Searles Lake IR6+7me
0.4
0.5
0.6
0.7
0.8
T2 H11
T1 H1
Searles Lake BIT
1.0
0.8
0.6
0.4
Searles Lake %GDGT-0
100
80
60
40
Devils Hole water table elevation (m)
8
6
4
2
0
MIS 1
MIS 2
MIS 3
MIS 4
MIS 5
MIS 6
MIS 7
0
25
50
75
100
125
150
175
200
Age (kyr)

Figure 7.

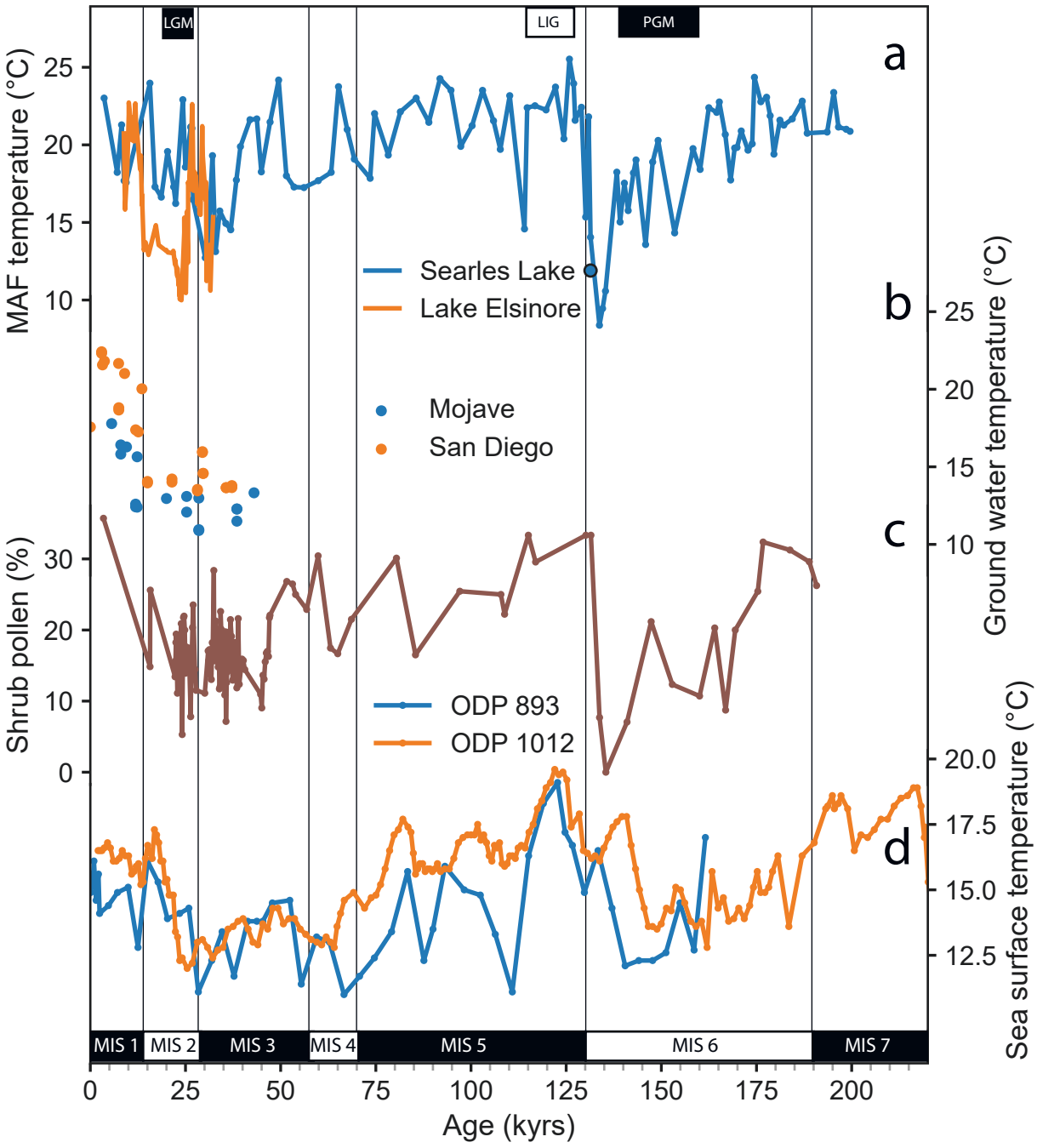
LGM
LIG
PGM
a
b
c
d
MAF temperature (°C)
Searles Lake
Lake Elsinore
Mojave
San Diego
Ground water temperature (°C)
Shrub pollen (%)
ODP 893
ODP 1012
Sea surface temperature (°C)
MIS 1
MIS 2
MIS 3
MIS 4
MIS 5
MIS 6
MIS 7
Age (kyrs)

Paleoceanography and Paleoclimatology

Biomarker and pollen evidence for late Pleistocene pluvials in the Mojave Desert

Mark D. Peaple[1], Tripti Bhattacharya[2], Tim K. Lowenstein[3], David McGee[4], Kristian J. Olson[3], Justin S. Stroup[5], Jessica E. Tierney[6], Sarah J. Feakins[1]

[1]Department of Earth Sciences, University of Southern California, Los Angeles, CA 90089

[2]Department of Earth and Environmental Sciences, Syracuse University, Syracuse NY 13210

[3]Department of Geological Sciences and Environmental Studies, State University of New York, Binghamton, New York 13902, USA

[4]Department of Earth, Atmospheric and Planetary Sciences, Massachusetts Institute of Technology, Cambridge, MA 02139

[5]Department of Atmospheric and Geological Sciences, State University of New York at Oswego, Oswego, NY 13126

[6]Department of Geosciences, University of Arizona, Tucson, AZ 85721

Contents of this file

Supplementary methods

Extended palynology methods

An initial set of 115 pollen analyses were performed at the U.S. Geological Survey's Florence Bascom Science Center in Reston, VA by Ronald Litwin and Nancy Durika. To extract pollen, 2–12 g of wet sample were initially washed using deionized water to remove salts. Sediments were then decalcified using HCl, and siliciclastic material was removed using HF and heavy liquid separation in $ZnCl_2$, and mounted in glycerin jelly. One calibrated tablet of exotic *Lycopodium clavatum* spores (62,712,2081 spores per tablet) was added to each sample to enable calculation of absolute pollen concentrations and pollen accumulation rates.

A subsequent set of 115 samples were processed at Syracuse University and the University of California, Berkeley's Quaternary Paleoecology Laboratory. We sampled 2 g of dry weight from each sample, added a tablet of *Lycopodium clavatum,* and used deionized water washes to dissolve salts and disaggregate samples, then subjected the sample to HCl and HF acid digestion, following by KOH to remove organic acids, and acetolysis. Samples were stained with safranin and suspended in silicone oil. We processed 2–3 samples using both methods, and found no systematic offsets in the pollen counts yielded by each method.

Modern plant study

As a complement to the downcore plant wax compound specific isotope work presented in the main paper, we provide a supplementary study of representative taxa in modern vegetation. These plant samples and lipid extractions were described previously (Peaple et al., 2021). They are newly analyzed for compound specific carbon and hydrogen isotopic composition for this study, using the same isotopic methods described in the main text. We studied representative desert shrub vegetation in Searles Valley (SV) including C_3 creosote bush, *Larrea tridentata* (n = 2) and rabbit brush, *Ericameria nauseosa* (n = 1) as well as C_4 saltbush (*Atriplex hymenelytra, Atriplex confertifoli* and *Atriplex canescens* n = 4). From the valley slopes we sampled the C_3 wild buckwheat, *Eriogonum pusillum* (n = 1) and spiny menodora, *Menodora spinescens* (n = 1) as well as the Crassulacean Acid Metabolism (CAM) prickly pear*, Opuntia chlorotica* (n = 1). We sampled conifers at 2150 m asl from the San Bernardino Mountains (SBM), CA (165 km to the south of Searles Lake) including: jeffrey pine, *Pinus jeffreyi* (n = 9)*;* western juniper, *Juniperus occidentalis* (n = 4)*,* and white fir (*Abies concolor*) (n = 3).

Supplementary results

Modern plant survey

As context for the downcore plant wax isotope distributions (**Figure S1a, b**), we report $\delta^{13}C$ and δD values for dominant homologues of the long chain *n*-alkanoic acids and *n*-alkanes in a survey of living plants (**Figure S1c, d**). The availability of isotopic data varies as the molecular abundance distributions differ between species.

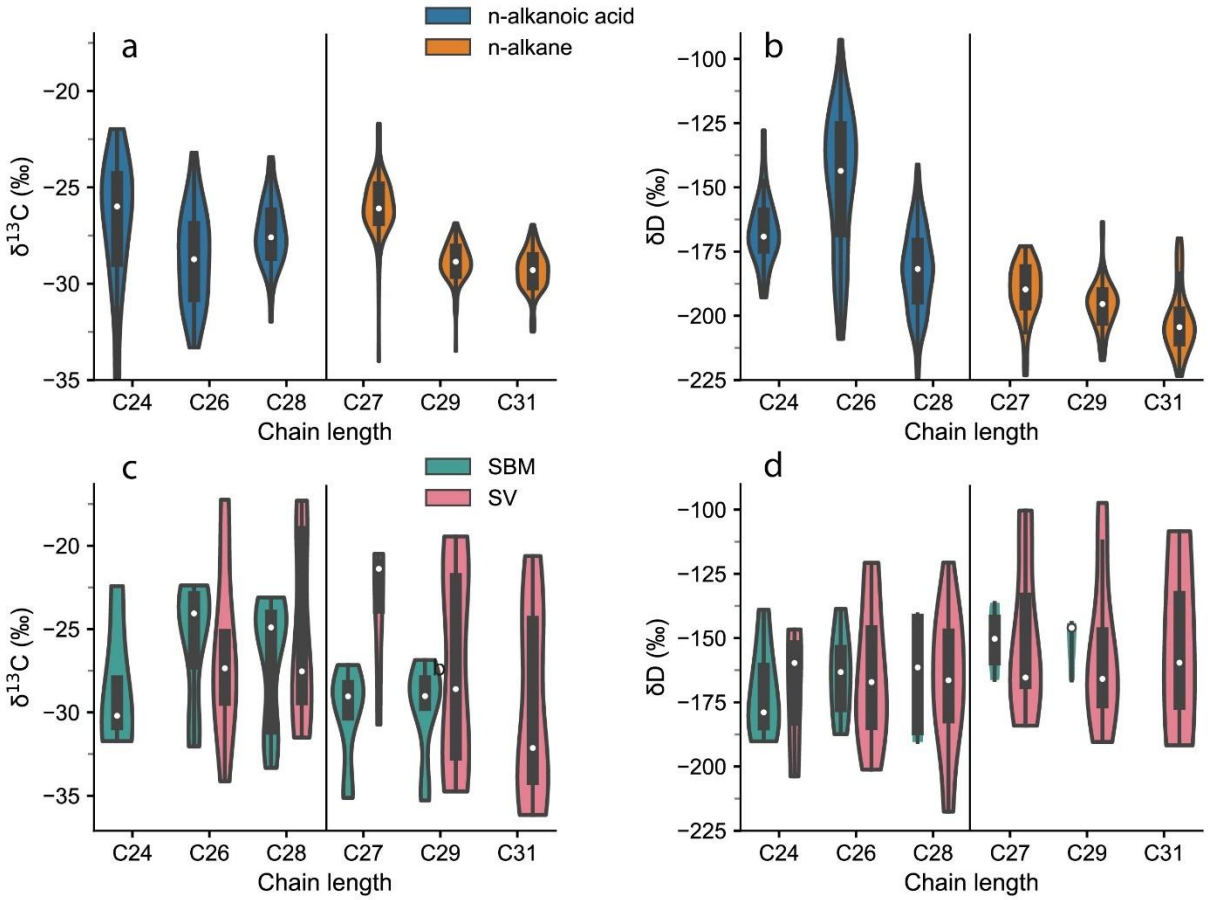

Figure S1. Violin plots showing a) $\delta^{13}C$ and b) δD values *n*-alkanoic acids (blue) and *n*-alkanes (orange) in SLAPP-SL17 and c) $\delta^{13}C$ and d) δD distributions for plants collected in the San Bernadino Mountain (SBM, green) and Searles Valley (SV, pink).

Carbon isotopes

The desert plant community from Searles Valley has a large range in carbon isotopic values indicating the use of C_3, C_4 and CAM pathways (Nobel and Bobich, 2002; Yu et al., 2019). Individual plants yielded $\delta^{13}C_{28acid}$ values ranging from -17.3‰ to 31.5‰ and $\delta^{13}C_{29alk}$ ranging from -20.3‰ to -34.7‰ (**Figure S1c, d**). The most negative values were measured in C_3 shrubs including *Menodora spinescens* ($\delta^{13}C_{29alk}$ = -32.5‰, $\delta^{13}C_{28acid}$ = -26.6‰, n = 1) and *Larrea tridentata* ($\delta^{13}C_{29alk}$ = -31.6‰, $\delta^{13}C_{28acid}$ = -28.3‰, n = 1). Cacti including *Opuntia chlorotica* ($\delta^{13}C_{28acid}$ = -19.7‰, $\delta^{13}C_{29alk}$ = -20‰, n = 1) and *Cylindropuntia bigelovii*

($\delta^{13}C_{28acid}$ = n.d. $\delta^{13}C_{29alk}$ = -19.4‰, n = 1) have values denoting use of Crassulacean Acid Metabolism (CAM). CAM plants are today a minor component of the mixed shrub cover and are likely at their maximum prevalence (arid conditions); as their carbon isotopic compositions are intermediate between the C_3 and C_4 plants, they are not explicitly considered for sedimentary contributions. We detect significant and varying contribution of C_4 xerophytic and halophytic taxa both in the pollen and in $\delta^{13}C$ downcore. High $\delta^{13}C$ values were measured in *Atriplex* (mean $\delta^{13}C_{28acid}$ = -18.2‰, $\delta^{13}C_{29alk}$ = -21.7‰, n = 1) using the C_4 pathway.

In conifers in North America, *n*-alkanoic acids are usually more abundant than *n*-alkanes (Diefendorf et al., 2015) as corroborated by sampling of pine and fir species present in the San Bernardino Mountains today, where C_{31} *n*-alkanes were rarely detectable. Thus conifers are unlikely to contribute to the *n*-alkane downcore record, with the exception of junipers which have high concentrations of C_{31}-C_{35} *n*-alkanes (Peaple et al., 2021). For the dominant *n*-alkane homologs: *Juniperus occidentalis* $\delta^{13}C_{33alk}$ (mean -31.3‰, 1σ = 0.8‰, n = 5), $\delta^{13}C_{29alk}$, *A. concolor* (mean -28.1‰, 1σ = 0.98‰, n = 3) and $\delta^{13}C_{29alk}$ *Pinus jeffreyi* (mean -28.6‰, 1σ = 0.7‰, n = 9). We report data for the C_{28} *n*-alkanoic acid homolog, often modal in plants, and reported downcore. We find $\delta^{13}C_{28acid}$ range from -32.4 to -23.1‰. *J. occidentalis* had the lowest mean $\delta^{13}C_{28acid}$ of -29.6‰ (1σ = 3.2‰, n = 4); *A. concolor* had a mean of -24.7‰ (1σ = 0.2‰, n = 3) and *P. jeffreyi* a mean of -24.4‰ (1σ = 1.1‰, n = 9). These conifers' abundant fatty acids may dominate the leaf wax transport in episodic montane runoff as seen in the Lake Elsinore catchment (Feakins et al., 2019). Our compound class comparison in modern species shows that the fatty acids are more abundant in conifers as expected, and also more enriched. We show the $\delta^{13}C_{acid}$ in these species are very enriched for C_3 plants, with values of -24 to -25‰ measured in these C_3 conifers growing at 2 km (**Figure S1c**), values that could easily be misconstrued for a C_3-C_4 mixture, when measured downstream in fluvial sediments or lakes.

Hydrogen isotopes

San Bernardino Mountain (SBM) conifers yielded δD_{28acid} values from -155‰ to -190‰ with a mean of -166‰. δD_{28acid} mean values for individual species were determined for *J. occidentalis* (-160‰, n = 1), *P. jeffreyi* (-186‰, 1σ = 5‰, n = 3) and *A. concolor* (-155‰, n = 1) and co-occurring *Artemisia tridentata* (-142‰, 1σ = 0.8‰, n = 2). Although the conifers do not have abundant *n*-alkanes, the angiosperm shrub *A. tridentata* yields δD_{29alk} (-152‰, 1σ = 10‰, n = 3). Desert plant taxa sampled in Searles Valley (SV) have δD_{28acid} values ranging from -121‰ to -217‰ (mean = -163‰, 1σ 23‰, n = 15) and δD_{29alk} ranging from -98‰ to -190‰ (mean = -155‰, 1σ =25‰, n = 13).

We found no systematic offset in hydrogen isotopic compositions between photosynthetic pathway (C_3, C_4 and CAM in order of prevalence on the landscape) suggesting that an apparent fractionation correction for the C_3 versus C_4 proportions is unlikely to be appropriate. The conifers had a smaller range in $\delta D_{C28acid}$ than the desert plants (35‰ vs 95‰) which could reflect the greater diversity of plant types (i.e shrubs, grasses and cacti) sampled in the Mojave Desert. δD_{C29alk} shows a similar distribution compared to $\delta D_{C28acid}$ in desert plants (**Figure S1**) although the mean value is slightly more enriched (-155‰ vs -166‰). Among the SBM vegetation we find a large range between δD_{C31alk} measured in *J. occidentalis* compared to the δD_{C29} measured in *A. tridentata* (-77‰ vs -152‰). This might reflect different water uptake

strategies of the plants, as junipers uptake water throughout the year and respond quickly to even small summer precipitation events (Williams and Ehleringer, 2000). However, we do not see similarly enriched $\delta D_{C28acid,}$ perhaps consistent with reports of seasonal offsets in production of *n*-alkanes and *n*-alkanoic acids in conifers (Freimuth et al., 2017).

Sediment core plant wax isotopic results

In the main text we report two homologues, here we show results for additional compounds in the homologous series as distributions (**Figure S1**) and downcore (**Figure S2**).

Carbon isotopes

For the *n*-alkanes (**Figure S1a**), $\delta^{13}C_{C27alk}$ ranges from -34.0‰ to -21.7‰ (mean -26.0‰), $\delta^{13}C_{29alk}$ ranges from -33.5‰ to -26.9‰ (mean -28.9‰) and $\delta^{13}C_{31alk}$ ranges from -32.5‰ to -27.0‰ (mean -29.4‰). $\delta^{13}C_{27alk}$ has a moderate positive correlation with $\delta^{13}C_{C28acid}$ (r = 0.64), although the correlations with the shorter chain $\delta^{13}C_{C26acid}$ and $\delta^{13}C_{24acid}$ are lower (r = 0.2, r = 0.38 respectively). The correlations between $\delta^{13}C_{28acid}$ and the longer chain $\delta^{13}C_{29alk}$ and $\delta^{13}C_{31alk}$ are moderate (r = 0.45 and r = 0.4 respectively). There is no correlation between the long chain $\delta^{13}C_{31alk}$ and the shorter chain $\delta^{13}C_{26acid}$ and $\delta^{13}C_{24acid}$ (r = 0.12 and r = 0.15 respectively). There is a strong correlation between $\delta^{13}C_{27alk}$ and $\delta^{13}C_{29alk}$ (r = 0.82) and between $\delta^{13}C_{29alk}$ and $\delta^{13}C_{31alk}$ (r = 0.78) although there is a weaker correlation between $\delta^{13}C_{27alk}$ and $\delta^{13}C_{31alk}$ (r = 0.64) indicating a difference in sourcing. For the *n*-alkanoic acids (**Figure S1a**), $\delta^{13}C_{24acid}$ ranges from -38.5‰ to -22‰, $\delta^{13}C_{26acid}$ ranges from -33.3‰ to -23.2‰ and $\delta^{13}C_{28acid}$ ranges from -32.0‰ to -23.4‰ with a mean of -27.4‰.

Hydrogen isotopes

For the hydrogen isotopic composition of the *n*-alkanes, both δD_{31alk} and δD_{29alk} show very similar trends downcore (**Figure S2c**), in addition to having similar means (-202‰ and -196‰ respectively) and ranges (-223‰ to -170‰ and -217‰ to -164‰ respectively, **Fig S1b**). δD_{27alk} is more enriched on average (mean = -190‰) but has a similar amplitude of variability (-223‰ to -173‰). For the *n*-alkanoic acids (**Figure S1b**), C_{28} homologue, $\delta D_{C28acid}$ ranged from -227‰ to -141‰ with a mean of -182‰. δD_{26acid} has a larger range (-209‰ to -92‰) and is on average more enriched (mean = -148‰) than δD_{28acid}, as is δD_{24acid} which ranges from -192‰ to -128‰ with a mean of -167‰. There is a positive correlation between the hydrogen isotopic compositions by *n*-alkanoic acid chain length, with the strongest correlation between δD_{26acid} and δD_{28acid} (r = 0.6) (**Figure S2d**). There is no correlation between the C_{31} *n*-alkanes and C_{28} *n*-alkanoic acids (r = 0) indicating different sources of these molecules.

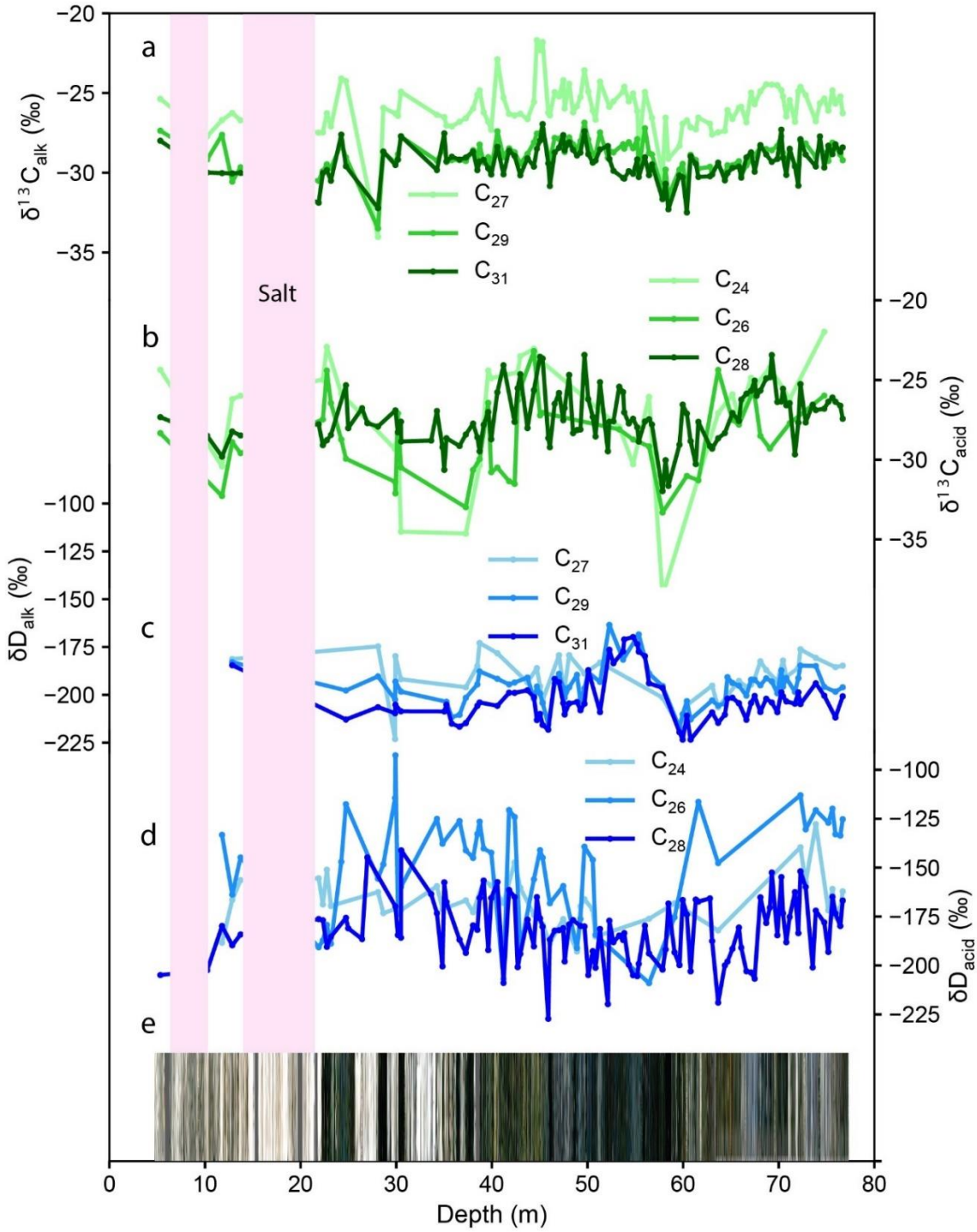

Figure S2. Changes in isotopic composition of *n*-alkanes and *n*-alkanoic acids with depth in SLAPP-SL17 core a) $\delta^{13}C$ measured from the C_{27}, C_{29} and C_{31} alkane chain lengths. b) $\delta^{13}C$ measured from the C_{24}, C_{26} and C_{28} alkanoic acid chain lengths. c) δD measured from the C_{27}, C_{29} and C_{31} alkane chain lengths. d) δD measured from the C_{24}, C_{26} and C_{28} alkanoic acid chain lengths. E) Composite core photo showing presence of muds (dark) and salts (white) downcore. Thick salt accumulations without biomarker sampling (pale pink shading).

Interpretation

Given the strong correlations between the C_{29} and C_{31} alkanes in both δD and $\delta^{13}C$ (**Figure S2a, C**) it is likely that they have a similar source. Even though bacteria and macrophytes have been recorded as producing long chain alkanes (Aichner et al., 2010; Makou et al., 2018), terrestrial plants are likely to be the dominant producers in most settings and thus we interpret C_{29alk} and C_{31alk} as having a terrestrial plant origin. The mean $\delta^{13}C$ of both C_{29alk} and C_{31alk} as well as the small range downcore (**Figure S2a**) suggests that these chain lengths have a C_3 source that is relatively invariant through time. Previous pollen studies from Owens Lake (Litwin et al., 1999; Woolfenden, 2003) in addition to pollen data presented here (**Figure S3a**) find that Artemisia and Juniper were the dominant plants in SV and thus we assume that these plants dominate contributions to C_{29alk} and C_{31alk}. The proportion of Amaranth pollen covaries with $\delta^{13}C_{29alk}$ and $\delta^{13}C_{31alk}$ (**Figure S3d**) suggesting that C_4 desert plants also contribute.

C_{24acid} and C_{26acid} likely had a different source to the long chain *n*-alkanes given the lack of correlation between their respective $\delta^{13}C$ and δD. The very negative $\delta^{13}C_{24acid}$ between 56 m to 60 m (-38.5‰), combined with the inferred fresher water conditions (**Figure S2d**) during this interval could imply that there is C_{24acid} algal input, as algae have been recorded as having lipid $\delta^{13}C$ as low as -40‰ (McCallister and Del Giorgio, 2008), and no measured modern terrestrial plants in this study have such low $\delta^{13}C_{acid}$ values (**Figure S1a**). The lack of such depleted $\delta^{13}C_{24acid}$ values in the rest of the core could suggest that algae production was suppressed by the higher water salinities and thus the relative contribution of algae C_{24acid} decreased. Throughout the rest of the core other macrophyte and terrestrial plant inputs likely contribute C_{24acid} to Searles Lake and as such the source of C_{24} is interpreted as changing downcore. The very enriched values of δD_{26acid} relative to other *n*-alkane and *n*-alkanoic acid chain lengths and the moderate positive correlation between δD_{26acid} ACE ($r = 0.4$) suggests that the source of C_{26acid} was living in Searles Lake/Owns Lake and thus the δD_{26acid} likely reflects both the δD of lake water in addition to the salinity of the lake water which modulates the fractionation between water and lipid (Sachse et al., 2012). Given that we see an increase in δD_{26acid} in association with an increase in lake salinity implies an algal source, as bacteria and algae epsilon decreases with increases in salinity (Sachse et al., 2012) whereas macrophyte fractionation increases with increasing salinity (Aichner et al., 2017).

$\delta^{13}C_{28acid}$ and $\delta^{13}C_{27alk}$ as well as δD_{28acid} and δD_{27alk} covary in the core and thus C_{28acid} and C_{27alk} likely share a similar source. Both $\delta^{13}C_{28acid}$ and $\delta^{13}C_{27alk}$ show a similar down core trend to the longer chain (C_{29alk}, C_{31alk}) alkane $\delta^{13}C$, although they are more enriched by 1.5-6‰. Additionally, whilst there is a strong correlation between δD_{28acid} and δD_{27alk} ($r = 0.7$) as well as a strong correlation between δD_{27alk} and both δD_{29alk} and δD_{31alk}, there is no correlation between $\delta D_{C28acid}$ and either δD_{29alk} or δD_{31alk}. This suggests that the δD_{27alk} is receiving lipid sourced from both the producers of long chain *n*-alkanes (terrestrial plants) as well as aquatic/microbial producers. C_{28} *n*-alkanoic may include a mixture of aquatic and terrestrial plant sources, given the moderate correlations between the δD and $\delta^{13}C$ of C_{28acid} and both mid chain length alkanes (C_{27alk}) and mid length chain alkanoic acids (C_{26acid}). The lack of correlation between the δD_{28acid} and δD_{31alk} indicates a difference in the signals captured by these two compound classes in Searles Lake. The δD_{28acid} is puzzling as it records D-enrichment during glacials, opposite to hydroclimate expectations, suggesting the producers of

n-alkanes and *n*-alkanoic acids differ. δD_{28acid} anticorrelates with pines (Figure 3), likely reflecting their abundant production of fatty acids. During the LGM (locally termed the Tioga glaciation), the upper limit of tree production descended from 3.5 to 2.5 km as glaciers and snowpack accumulated (Moore and Moring, 2013). The elimination of the highest elevation conifer forests during glacials could increase the δD value of exported plant wax *n*-alkanoic acids by at most 10‰ based on the expected altitude effect (Feakins et al., 2018). A glacial expansion of lowland conifers could further add D-enriched lowland production. However, it seems unlikely the altitude source effect could explain all of the 40‰ variability observed downcore (**Figure 2e**). Machine learning has suggested the possibility of aquatic macrophyte inputs (Peaple et al., 2021), although unverified locally, given the lack of modern surface water. There is some upstream macrophyte evidence from palynology of Owens Lake (Woolfenden, 2003), although none in Searles Lake (this study). The δD signal of aquatic production (whether by macrophytes or microbial production) would be affected by changing lake water δD as well as lake salinity effects on fractionation (Sachse et al., 2012). Input of snow and glacial melt to Searles Lake during interstadial periods would result in aquatic plants acquiring a partially lagged precipitation δD signal, which could obfuscate climatic interpretations. Snow melt could also have indirect effects influencing water table levels, which would impact the phreatophytic C_4 shrubs that use shallow groundwater. We do not see large changes in the δD_{28acid} or signal associated with glacial terminations which could suggest that snowmelt does not play a significant role in regulating lake δD. There is a correlation between $\delta^{13}C_{28acid}$ and $bayMBT_0$ temperature ($r = 0.48$, $p < 0.05$), possibly suggesting an increase in aquatic production under warmer conditions. Rather than attempt to further theorize about multiple unknowns, we suggest that both upland conifer and aquatic production may contribute alkanoic acids, confounding the $\delta D_{22\text{-}28acid}$ signal here. We therefore select the C_{31} *n*-alkane as a proxy for terrestrial vegetation and hydroclimate in the main text.

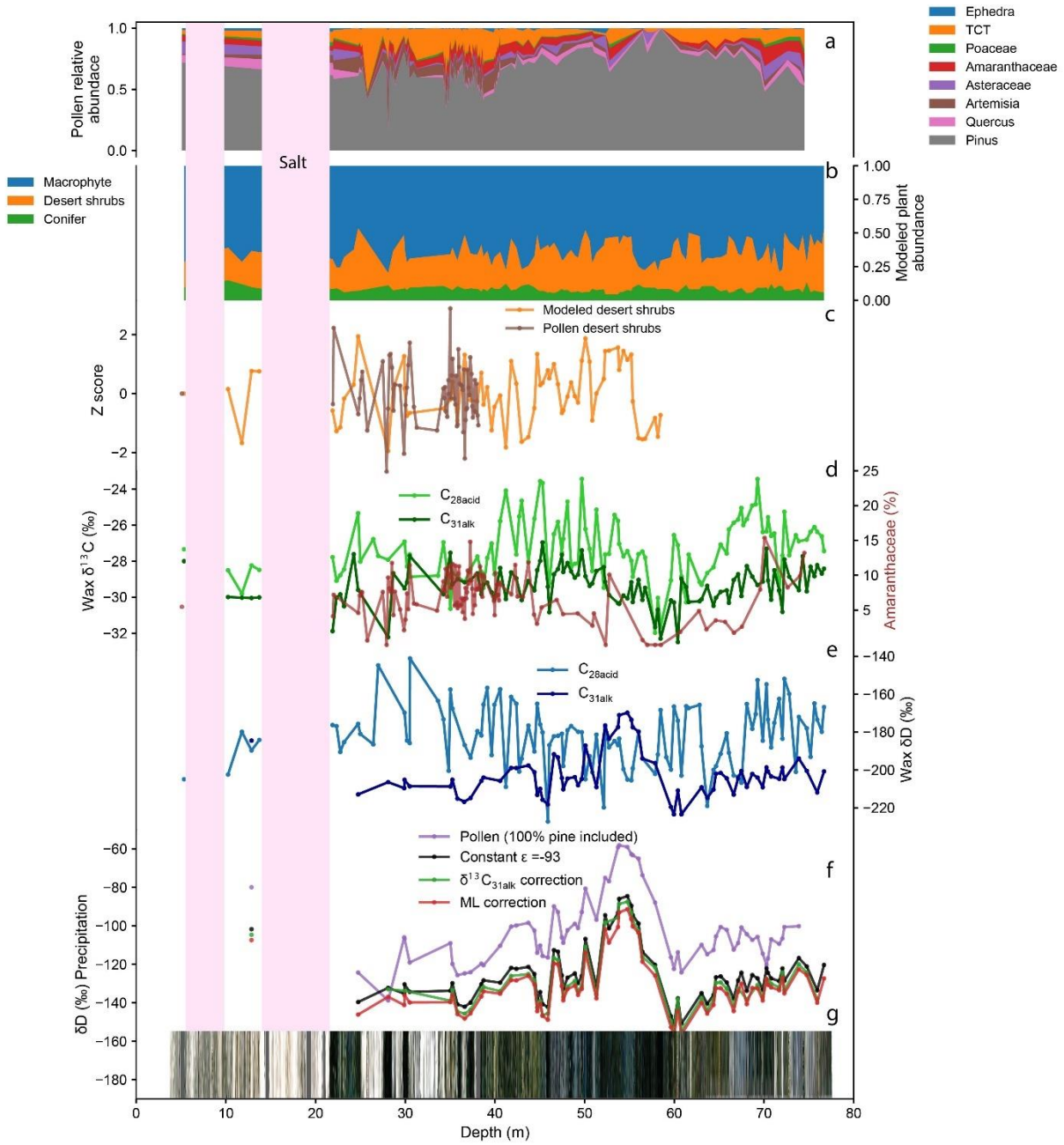

Figure S3. Downcore pollen and plant wax proxies from SLAPP-SRLS17. a) Proportion of pollen taxa. b) Modelled vegetation types based on SVM machine learning of plant wax distributions in modern taxa applied to the downcore record (Peaple et al., 2021). c) Comparison between modelled desert plant types and sum Amaranth and Asteraceae pollen. d) $\delta^{13}C_{28acid}$ and $\delta^{13}C_{31alk}$ compared to Amaranth pollen. e) δD_{28acid} and δD_{31alk}. f) Precipitation δD estimated from the δD_{31alk} with $\varepsilon_{wax/p}$ determined as: i) "constant" -93‰, or temporally varying as calculated based on the ii) "pollen" i.e., the proportion of pollen taxa in core, iii), "C_3 v. C_4" proportion based on $\delta^{13}C_{31alk}$, and iv) "ML" where "constant" is modified by mixing with the SVM modelled desert plant proportions from machine learning. g) Composite core photo. Thick salt accumulations without biomarker sampling (pale pink shading).

Modelling the apparent fractionation between plant wax and precipitation

The hydrogen isotopic composition of plant wax *n*-alkanes is of interest in order to reconstruct the hydrogen isotopic composition of precipitation, but that interpretation requires knowledge of the apparent fractionation between precipitation and plant wax in the modern system and an informed estimation for the past. The reconstructed precipitation isotopic composition is dependent upon the choice of apparent fractionation. In order to quantify the implications of interpretive choices, we assess the sensitivity of δD_{precip} to changes in $\varepsilon_{wax/p}$ estimated using four different methods (**Figure S3f**):

i. In the main text, we apply a "**constant**" ε_{C3} of -93‰, based upon modern plant water and plant wax *n*-alkane studies, that found a constant average fractionation of -93‰ for woody C_3 plants sampled across a W-E aridity gradient from the coastal and montane woodlands to the Mojave Desert (Feakins and Sessions, 2010). Apparent fractionations are relatively invariant in this range of climate and vegetation, supporting the simplest approach to downcore reconstructions here.

ii. Pollen corrections have been applied in a few studies (Feakins, 2013; Inglis et al., 2020; Tamalavage et al., 2020). We measured pollen and plant wax in parallel in the core, as sampling depths differ, the data were each first interpolated onto the same timestep using linear interpolation with a resolution of 1.7 kyr. The "**pollen**" approach calculates $\varepsilon_{wax/p}$ using a mixing model (**Figure S3f**) based on the relative proportion of pollen taxa, each assigned an epsilon from the literature, with the following equation:

$$\varepsilon_{wax/p\ \text{"pollen"}} = f_{pine} * \varepsilon_{pine} + f_{artemisia} * \varepsilon_{artemisia} + f_{asteraceae} * \varepsilon_{asteraceae+} \quad (1)$$
$$f_{amaranthaceae} * \varepsilon_{amaranthaceae} + f_{poaceae} * \varepsilon_{poaceae} + f_{juniper} * \varepsilon_{juniper}$$

Where pine epsilon = -128‰ (Tipple and Pagani, 2013), artemisia epsilon = -60‰ (Feakins, unpublished), asteraceae epsilon = -112‰ (Sachse et al., 2012), amaranthaceae epsilon = -81‰ (Sachse et al., 2012), poaceae epsilon = -134‰ (Sachse et al., 2012) and juniper epsilon = -89 (Tipple and Pagani, 2013). We determine a mean $\varepsilon_{wax/p}$ "pollen" of -113‰ which is close to the value assigned to the pine component (-128‰ which is the dominant pollen **Figure S3f**) but reduced by the smaller apparent fractionations of desert and juniper taxa. The downcore variation has a standard deviation of 6.5‰, a small vegetation effect, as assessed by pollen.

iii. Carbon isotopic corrections have been applied in tropical settings (Tipple and Pagani, 2010; Fornace et al., 2016; Windler et al., 2020) to account for different apparent fractionation for C_3 and C_4 vegetation types (Sachse et al., 2012) and this works well in the presence of tropical C_4 grasses with more strongly differentiated fractionations. The approach is tested here for xerophytic/halophytic C_4 woody shrubs. We assigned ε_{C3} of -93‰ denoting the apparent fractionation measured for C_3 woody vegetation surveyed across Southern California (Feakins and Sessions, 2010) and estimate the ε_{C4} component as -81‰ based on values reported for chenono-amaranth (n = 10 samples, Bi et al., 2005; Krull et al., 2006; Liu et al., 2006) from a global collation (Sachse et al., 2012). We measured hydrogen and carbon isotopes on the same samples in the SLAPP-SRLS17 sediment core, thus used the $\delta^{13}C_{31alk}$ values to determine the f_{C4} assuming that

main driver of $\delta^{13}C_{31alk}$ was the presence of C_4 plants, using a mixing model approach to generate a carbon-isotope informed $\varepsilon_{wax/p}$, "C_3 v C_4" as follows:

$$\varepsilon_{wax/p\ \text{“C3 v C4”}} = f_{1\text{-}C4} * \varepsilon_{C3} + f_{C4} * \varepsilon_{C4} \quad (2)$$

This mixing model has a mean epsilon of -89‰ 1σ = 1.0‰.

iv. Here we introduce a new approach to quantify the vegetation effect, and use the machine learning of plant wax *n*-alkane and *n*-alkanoic acid plant wax distributions in the dominant plant taxa and the downcore record (Peaple et al., 2021). The machine learning vegetation correction is based on the modelled proportion of vegetation using the SVM algorithm (Peaple et al., 2021). We assigned endmember fractionations for the desert plants, macrophytes and conifers categories, identified in the machine learning approach, as -81‰ (Sachse et al., 2012), -86‰ (Aichner et al., 2010) and -109‰ (Tipple and Pagani, 2013) respectively.

$$\varepsilon_{wax/p\ \text{“ML”}} = f_{desert} * \varepsilon_{desert} + f_{macro} * \varepsilon_{macro} + f_{conifer} * \varepsilon_{conifer} \quad (3)$$

This results in a mean epsilon of -86.8‰ 1σ = 0.7.

All four $\varepsilon_{wax/p}$ methods yield similar reconstructions (mean 1σ = 2.6) apart from the pollen correction (ii) which yields δD_{precip} estimates that are +20‰ offset compared to the other methods. We discount this pollen-based estimate (ii) because: a) the pollen record is dominated by pine, which is likely overrepresented due to the wind dispersed nature of its pollen and b) pines produce very little C_{31alk} thus a correction dominated by changes of pine is potentially spurious. We caution against the pollen correction method in *n*-alkane records in similar pine-pollen dominated assemblages. While we could weight to lower or eliminate the pine influence, our estimates by the other approaches indicate that this would only shift the absolute value and have limited influence on the downcore variability. We discount the mixing model approach (iii) due to the weakness of its assumption that changes in $\delta^{13}C_{31alk}$ would be driven solely by changes in the relative proportions of C_3 and C_4 plants. The approach is compromised here as both the changing moisture variability and changing proportions of conifers would affect the C_3 "endmember". We also reject the machine learning approach (iv) as the plant groups reconstructed using this method (conifers, desert plants and macrophytes) have large intra group ranges in epsilon which cannot be constrained. We thus apply the regionally-determined, constant apparent fractionation of -93‰ (i) to convert δD_{31alk} into an estimate of the δD value of precipitation (δD_{precip}) as reported the main text. We correct for the changing composition of seawater (source water for evaporation), due to changes in glacial ice volume using the benthic $\delta^{18}O$ stack (Lisiecki and Raymo, 2005), in order to evaluate changes in storm track and other regional climatic drivers of precipitation isotopic variability.

Supplementary palynology results

Glacial to interglacial changes in pollen taxa composition occur downcore, with shrubs and pines dominating glacial periods with Juniper and Artemisia expanding during cold glacial periods (**Fig S3a**). A Nonmetric Multi-Dimensional Scaling analysis confirms that pollen taxa composition is different during glacial and interglacial phases (**Fig S4a**). Changes in pollen taxa % could be impacted by changes in pollen influx rates to lakes (Pennington, 1979). We show that pollen influx rates show similar trends to pollen % composition (**Fig S3b, c, d**), suggesting that pollen taxa % reflects changes in catchment vegetation change.

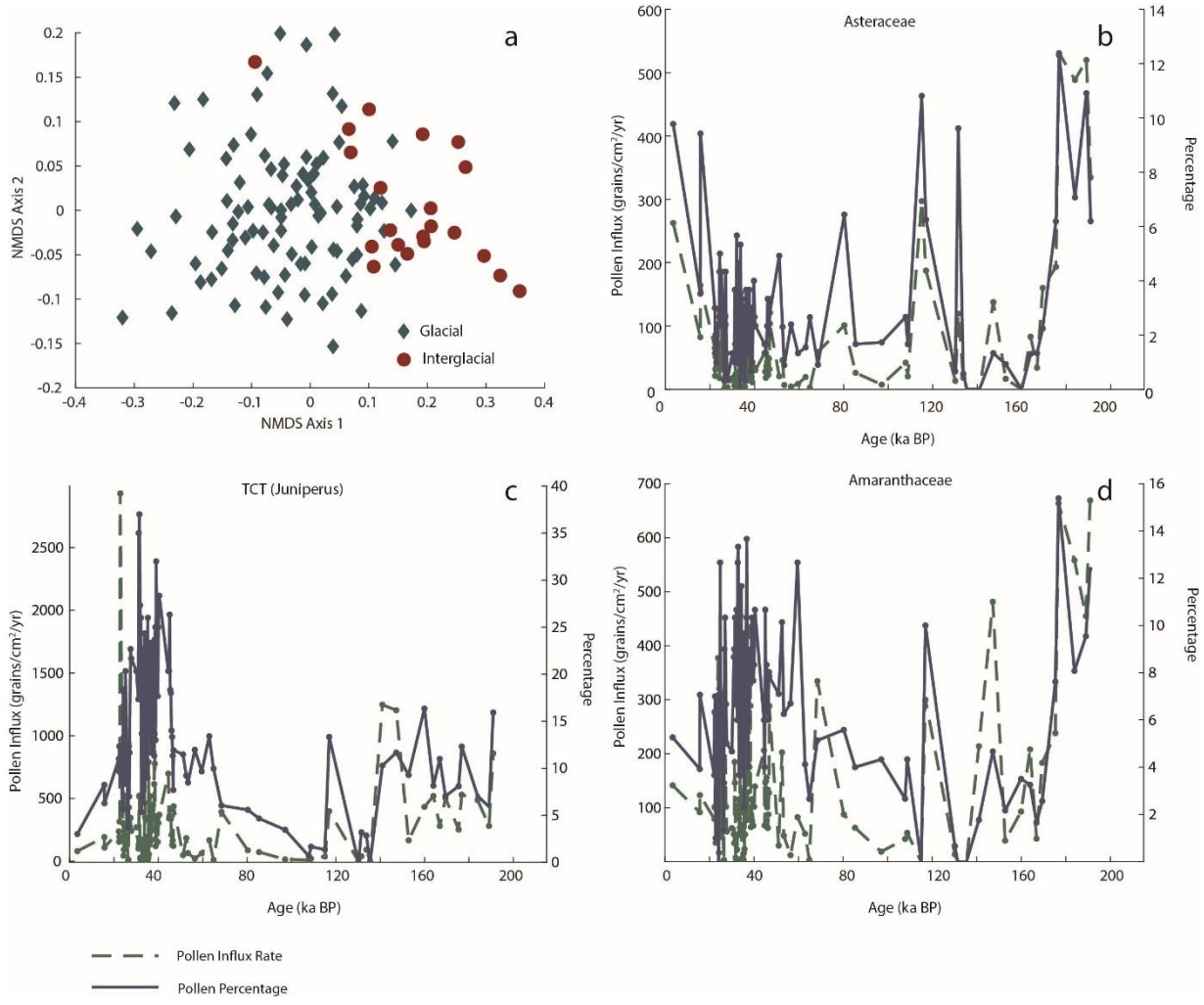

Figure S4. Analysis of major pollen taxa in SLAPP-SRLS17 sediment core. a) Non-metric multi-dimensional scaling (NMDS) analysis with glacial (blue diamond) and interglacial (red circle) samples highlighted. b, c, d) Time series plots showing the pollen percentage and influx rate.

GDGT concentrations and indices

GDGT distributions in stratigraphic context

We report the concentration of the br and isoGDGTs and select compounds on the sediment stratigraphic context (**Figure S5**). We find crenarchaeol has low concentrations (<1 ng/g) throughout the core except during the interval 57 to 58.5 m (highlighted in blue) where concentrations peak at 238 ng/g (**Figure S5a**). This depth interval also shows a peak in the ∑brGDGT concentration to 810 ng/g. Between 30 m to 76 m brGDGT concentrations are variable between 1 to 140 ng/g and between 6 m to 30 m brGDGT concentrations are lower and range from 1 to 11 ng/g. ∑isoGDGTs have peak concentrations between 44 m to 51 m, 57 m to 58.5 m and 65 m to 76 m, although unlike brGDGTs and crenarchaeol, ∑isoGDGTs have a maximum concentration between 65 m to 75 m with a peak concentration of 1015 ng/g. Like ∑brGDGT, ∑isoGDGT also have lower concentrations in the upper section of the core between 6 to 30 m likely due to the higher salinity conditions as shown by the salts in the SLAPP-SRLS17 sediment core and high ACE values. Salts have higher accumulation rates and thus greater dilution of organics and the environment is also more inhospitable to many organisms.

BIT and %GDGT-0 are uniformly high (>0.9) throughout much of the sediment sequence but both show decreases between 57 to 58.5 m. The low BIT and %GDGT-0 between 57 to 58.5 m is driven primarily by the increase in crenarchaeol concentration (**Figure S5b**) and represents and expansion in the amount of Thaumarcheota in the lake, likely in response to an increase in oxygen and a decrease in salinity.

Caldarcheaol (isoGDGT-0, **Figure 5c**) makes up the majority of the ∑isoGDGT (**Figure 5a**) and thus shows the same abundance trends with depth. Between 63 m to 76 m depth archaeol correlates with caldarchaeol ($r = 0.64$), although there is a lack of correlation between 6 m and 63 m ($r = 0$). There is peak in the archeaol at 35 m where concentrations reach 909 ng/g and occur in muds interbedded in salts, suggesting hypersaline lake conditions.

ACE (**Figure S5d**) is driven by changes in the relative proportion of archeaol and caldarchaeol (isoGDGT-0, **Figure S5c**). ACE is variable with depth, ranging from 1 to 99, representing fresh water to water salinities > 300 psu (Turich and Freeman, 2011). Low ACE values are recorded in association with mud layers, with higher ACE seen from sections containing interbedded salts (**Figure S5g**). This can be seen visually in the core; between 33 to 50 m ACE decreases from 95 to varying between 40 to 2 and this matches the change from interbedded mud and salt layers to massive mud.

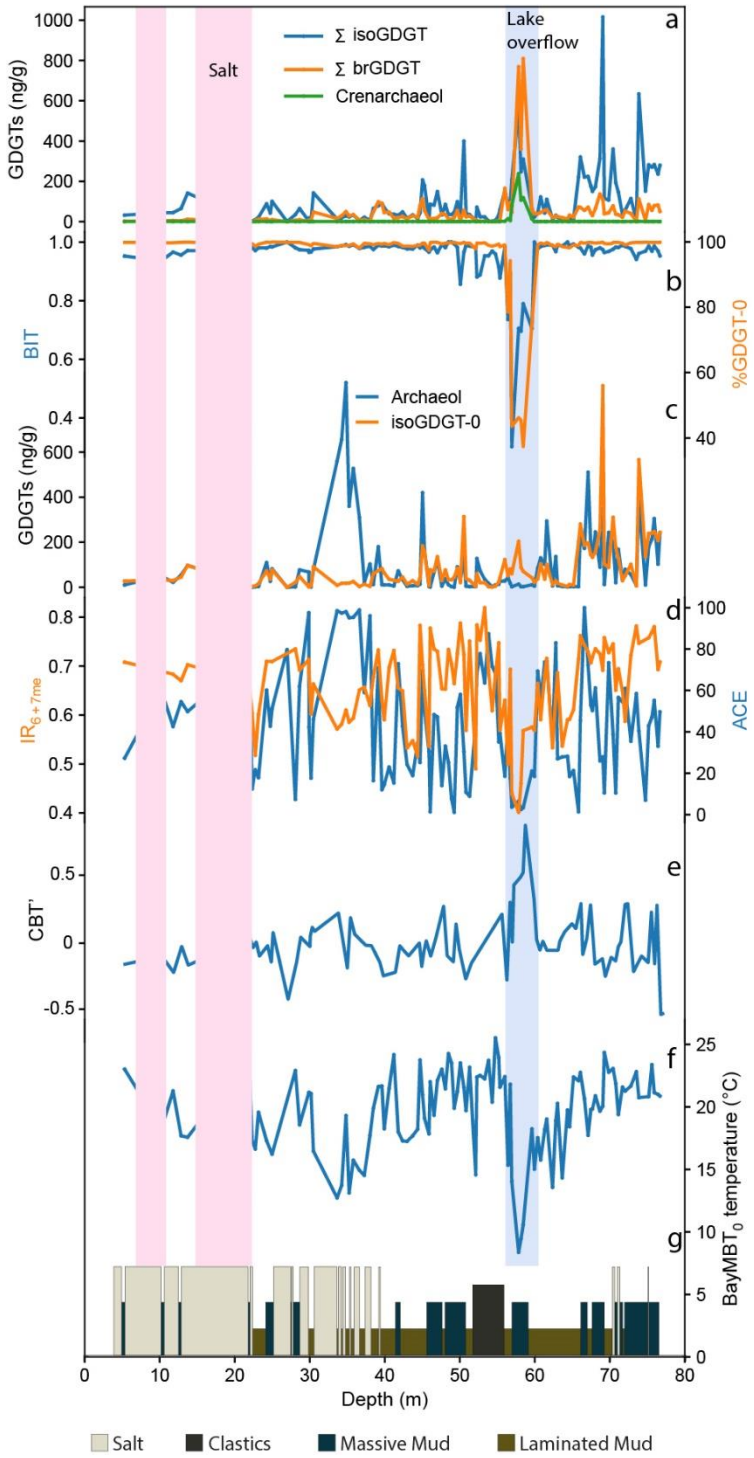

Figure S5. Downcore GDGT concentrations and indices in SLAPP-SRLS17, showing concentrations of a) summed and select GDGTs concentrations, b) BIT and %GDGT-0, c) caldarchaeol and isoGDGT-0, d) ACE and IR_{6+7me} index for salinity, e) CBT', f) reconstructed MAF temperatures and g) composite core stratigraphic column. Overflowing lake conditions with mud facies and low ACE salinity (blue shading) occurred during Termination 2 (T2), associated with high productivity (a) and a well-mixed lake (b). Thick salt accumulations without biomarker sampling (pale pink shading).

Evaluation of two salinity proxies

To determine the relationship between the two salinity proxies ACE and IR_{6+7me}, based on Archaea and Bacteria respectively, we present a cross-plot and highlight the agreement at low and high salinity and the challenge with mid-range salinity detection with either proxy (Figure S6).

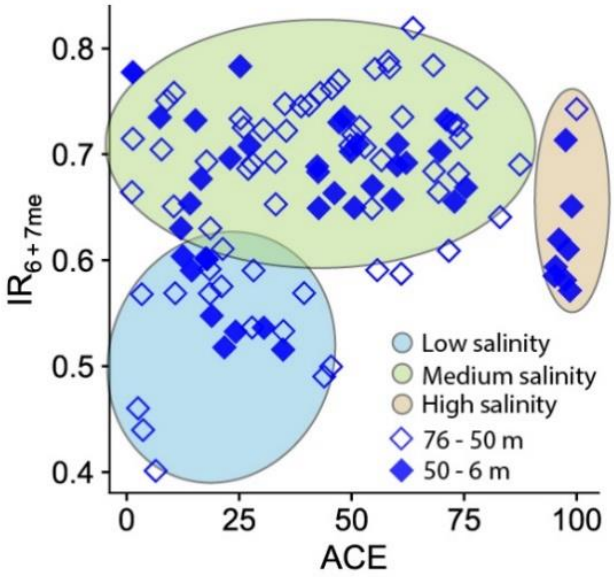

Figure S6 – Cross plot of ACE and IR6+7me measured in the same samples. The region where both ACE and IR_{6+7me} are low (blue shading) represents lower salinity samples. The region with high IR_{6+7me} but with ACE <0.85 (green shading) represents medium salinity samples and the region with ACE > 0.85 represents high salinity samples. Open diamonds represent samples above 50 m core depth and filled diamonds represent samples below 50 m core depth.

We also compare their time series (**Figure S7a**) cross wavelet spectra (**Figure S7b**) and frequency spectra (**Figure S7c**). Both salinity proxies show precessional pacing, showing both share a common signal of salinity variations, in contrast to the obliquity-dominated δD_{precip} (**Figure S5c**). Cross spectral analysis shows both salinity proxies have phase coherence in the precessional and obliquity bands (1/19–1/45 kyrs) between 175–90 kyrs (**Figure S5b**). Substantial precessional variability is also present in the % total organic matter measured in Baldwin Lake (Southern California) sediments, between 125–75 kyrs (Glover et al., 2017), suggesting changes in summer insolation were important in controlling regional water balance during MIS6–MIS5. We find higher frequency coherence between 1/10–1/17 kyrs than 90–50 kyrs and weaker antiphase coherence between 50–12 kyrs at Searles (**Figure S5b**).

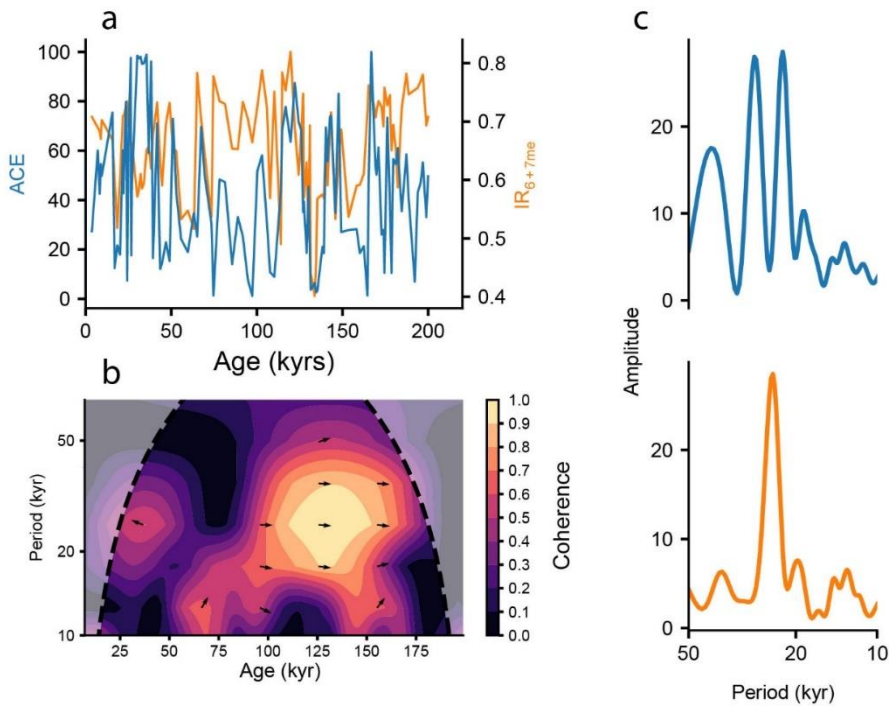

Figure S7. Time and frequency response of salinity proxies ACE (blue) and IR_{6+7me} (orange). a) Time series of ACE and IR_{6+7me} b) Wavelet coherence between ACE and IR_{6+7me}. c) Weighted wavelet Z transform frequency spectrum of ACE (blue) and IR_{6+7me} (orange).

Temperature

The $BayMBT_0$ temperature calibration (Martínez-Sosa et al., 2021) applied to the measured MBT'_{5Me} downcore yields months above freezing (MAF) between 7 to 25°C (**Figure S5f**). MBT'_{5Me} decreased between 76 to 57 m to a minimum of 7°C when Searles Lake is interpreted to have overflowed into Lake Panamint. MBT'_{5Me} then rapidly increased to higher temperatures (23-25°C) between 56 to 40 m. Temperatures then decreased between 40 to 30 m to 12-15°C in association with the appearance of salts in the core. Temperatures were variable between 30 to 6 m and ranged from 15-23°C, with a cooler period of 16-17°C occurring between 22 to 26 m in association with mud deposits. There is a positive association between $BayMBT_0$ temperature and the presence of desert shrub pollen in the core which suggests that in spite of the hypersaline and hyperalkaline lake chemistry the MBT'_{5Me} is primarily responding to changes in water temperature.

In order to interrogate the choice of calibration, we compared compilations of soil (Dearing Crampton-Flood et al., 2020) and lake brGDGTs (Martínez-Sosa et al., 2021) filtered to only consider those between 25 – 14 °C equivalent to the temperature range experienced in Searles Valley (**Figure S8**). This lends confidence in the choice of lake temperature calibration for temperature reconstructions. This test also indicates that the salinity variations do not yield a community of producers with a different brGDGT distribution, which is reassuring as salinity can lead to "warm" biases in some lakes including nearby Mono Lake (Martinez Sosa et al., 2021).

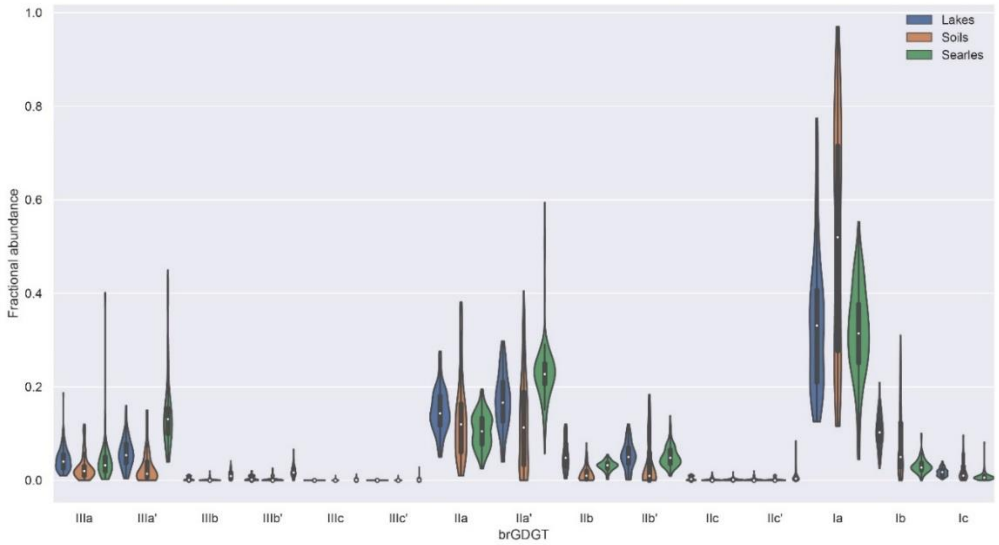

Figure S8. Violin plots of brGDGT distributions from soil (Dearing Crampton-Flood et al., 2020) and lake (Martínez-Sosa et al., 2021) compilations, selecting those entries with MAT of 14–25 °C, for comparison to brGDGT distributions from Searles Lake SLAPP samples. Searles appears to have lake-like distributions.

We also calculate the IIIa/IIa index used to determine the source of brGDGTs, with soils typically having lower IIIa/IIa compared to lacustrine brGDGTs (Xiao et al., 2016), where

$$\text{IIIa/IIa} = (\text{IIIa}+\text{IIIa}')/(\text{IIa}+\text{IIa}') \quad (4)$$

We compared the distributions of Searles Lake IIIa/IIa with the global compilations of lacustrine and soil IIIa/IIa values and found that Searles Lake IIIa/IIa were more similar to lacustrine values (**Figure S9**). The relative proportion of tetramethyl, pentamethyl and hexamethyl measured in Searles Lake samples is more similar to the distribution of lacustrine samples than the soil samples (**Figure S10**). These tests indicate the dominant source of brGDGTs to Searles Lake were bacteria living in the lake, and thus brGDGT distributions likely record lacustrine conditions (**Figures S8-10**).

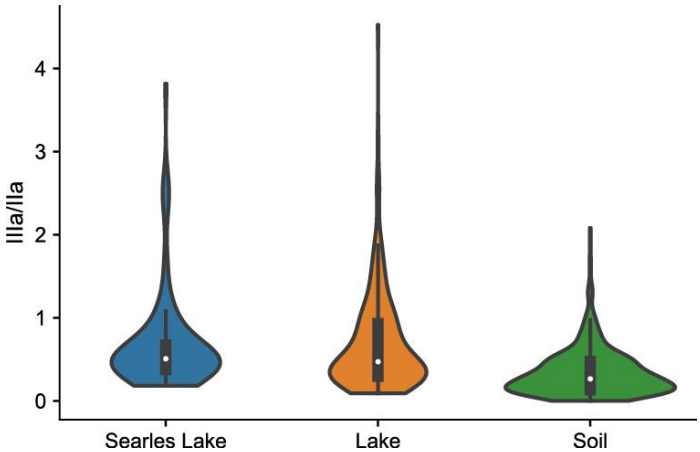

Figure S9. Violin plots of distributions of IIIa/IIa from soil (Dearing Crampton-Flood et al., 2020) and lakes (Martínez-Sosa et al., 2021). Searles appears to have lake-like distributions.

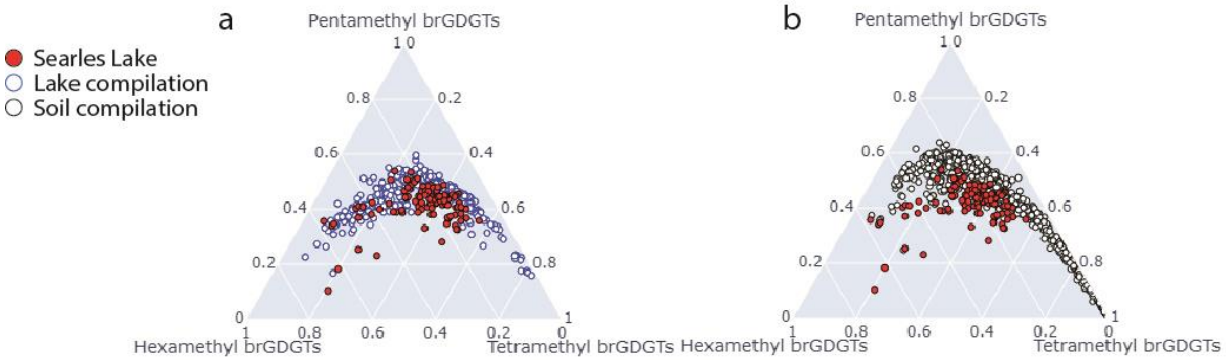

Figure S10. Ternary phase diagrams showing the proportion of tetramethyl, pentamethyl and hexamethyl brGDGTs from Searles Lake sediments, soils (Dearing Crampton-Flood et al., 2020) and lakes (Martínez-Sosa et al., 2021).

Assessing the effect of removing *Pinus* spp. pollen on the PCA analysis

The PCA analysis in the main text includes Pinus spp (Figure 3). Here we compare the effects of including or excluding *Pinus* spp. (Figure S11). Biomarker and pollen loadings are similar in both PCAs indicating that *Pinus* spp. pollen does not significantly affect the PCA analysis.

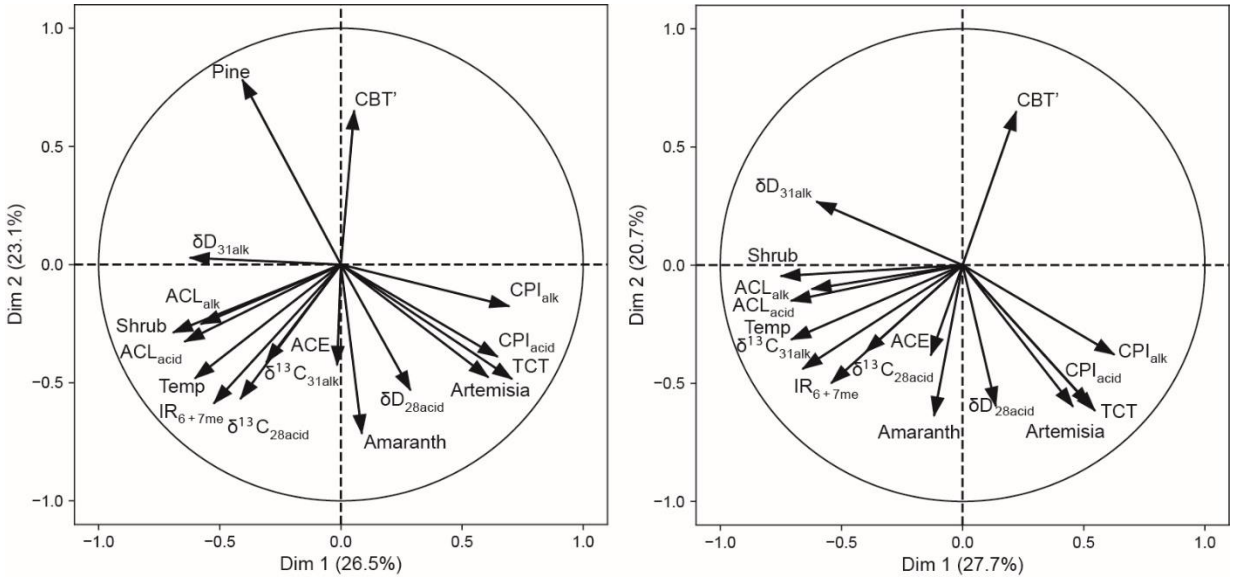

Figure S11. PCA to assess biomarker and pollen covariations (Shrub = sum of Amaranthaceae and Asteraceae pollen abundance). *Pinus* spp. pollen was included in Figure 3 PCA (left) and excluded in the PCA (right).